Characteristics of vortex shedding from a sinusoidally pitching hydrofoil at high Reynolds number

Xiaobo Zheng,[1] Stefan Pröbsting,[1] Hongliang Wang,[1] and Ye Li[1,2,3,4,*]
[1]*School of Naval Architecture, Ocean and Civil Engineering, Shanghai Jiao Tong University, 200240 Shanghai, China*
[2]*State Key Laboratory of Ocean Engineering, Shanghai Jiao Tong University, 200240 Shanghai, China*
[3]*Laboratory of Multiple Function Towing Tank, Shanghai Jiao Tong University, 200240 Shanghai, China*
[4]*Key Laboratory of Hydrodynamics (Ministry of Education), Shanghai Jiao Tong University, 200240 Shanghai, China*

(Received 14 February 2021; accepted 6 July 2021; published 9 August 2021)

The paper describes experiments on a sinusoidally pitching NACA 0012 hydrofoil with reduced frequency $0.16 \leqslant k \leqslant 2.51$ and angle of attack amplitude $6^\circ \leqslant \alpha_m \leqslant 34^\circ$. It extends the chord Reynolds number range with respect to earlier studies to $\mathrm{Re} = 5.9 \times 10^4$, 1.2×10^5, 1.9×10^5, and 2.4×10^5. Lift, drag, and moment are directly measured and compared with predictions from linear inviscid theory, while wake flowfields are visualized by phase-locked particle image velocimetry. Three vortex shedding regimes, i.e., the undulating wake, the reverse von Kármán vortex street, and the leading-edge vortex, are identified from the phase-averaged vorticity fields at different k and α_m. The nonlinear effect on statistical features of the force and moment responses gradually increases with α_m. The viscous effect leads to relatively large deviations of the measured responses from the linear inviscid models at low k. With increasing Re the measured values gradually approach those predicted by the models. Moreover, linear inviscid theory cannot capture the α_m-dependent behavior of the drag and moment phase lags ψ_d and ψ_m, respectively, resulting in a larger deviation from the measured values. A linear variation of ψ_m with α_m is found at k and Re for which the reverse von Kármán vortex street dominates. Within the trailing-edge shedding regimes of the undulating wake and the reverse von Kármán vortex street, the force and moment responses are largely insensitive to the wake pattern at varied α_m. However, in the leading-edge vortex regime, at low k and large α_m, the flow remains no longer attached and the time-dependent pitching moment is found to be strongly affected by the leading-edge vortex over the wing.

DOI: 10.1103/PhysRevFluids.6.084702

I. INTRODUCTION

Unsteady fluid dynamics of air- and hydrofoils has experienced sustained interest for several decades, because the unsteady loads on such foils are critical to the safety and performance of, e.g., turbomachinery, helicopter rotors, wind turbines, and tidal turbines [1–4]. Potential benefits of unsteady effects, such as optimizing propulsive efficiency, controlling periodic vortex generation, and delaying stall, have also been targeted in the design of modern fluid-dynamic vehicles and devices. Studies date back to the early works based on linearized thin-aerofoil theory by Theodorsen [5] (below referred to as Theodorsen's model) and Sears [6], who considered periodic oscillations of a foil in a uniform stream and periodic fluctuations in the approaching flow, respectively. By

*ye.li@sjtu.edu.cn

using the principle of conservation of angular momentum, i.e., the vortical impulse theory, von Kármán and Sears [7] developed general expressions for the force and moment. Garrick [8] studied the mean thrust and propulsive efficiency produced by a flapping aerofoil with three degrees of freedom including heave and pitch of an aerofoil and pitch of an aileron. Based on the analysis by Theodorsen [5] for unsteady lift and the analysis by von Kármán and Burgers [9] for the streamwise force, Garrick [8] also proposed a model for the drag response to sinusoidal oscillation (below referred to as Garrick's model).

The validity of these studies is limited by the assumptions of a thin foil (linearization) and potential flow. By considering the coupling effect between the unsteady disturbance and the steady-flow disturbance caused by the aerofoil geometry at an angle of attack (denoted by α), van Dyke [10] introduced second-order models. Later, McCroskey and Philippe [11] and McCroskey and Pucci [12] studied viscous effects and the viscous-inviscid interaction for the unsteady flow around the foil. The viscous effect was found to be significant with vortex formation and shedding, e.g., with the leading-edge vortex (LEV, which refers to the vortices that form and shed off the foil upstream of the trailing edge) during dynamic stall [3,13].

Recently, analytic-numerical coupling methods have seen developments adopting unsteady thin-aerofoil theory corrected by considering additional vortices [14–17] or an unsteady shear layer [18]. Unsteady forces were estimated using vortex force mapping methods [15,19] and vortical impulse integration [20–22]. While Garrick [8] considered only leading-edge suction, and the pressure force projected along the streamwise direction, Fernandez-Feria [20] employed vortical impulse theory to include the effect of wake vorticity over the entire surface (below referred to as Fernandez-Feria's model).

To gain a better understanding of highly efficient flyers and swimmers in nature, and to develop or improve models, a comprehensive set of experimental studies was reported [23–26]. Triantafyllou *et al.* [23] reviewed experimental studies on mechanisms of force production and the formation of vortical structures for oscillating bio-mimetic foils. Ol [27] reported particle image velocimetry (PIV) measurements and Yu *et al.* [28] reported force balance measurements studying the unsteady effects with the amplitude of angle of attack (denoted by α_m) up to 40° and 90°, respectively, but focusing at the pitch-ramp motion with α linearly increasing rather than the sinusoidal pitch. Relatively few investigations have been performed on the unsteady force response to sinusoidal foil oscillation under attached flow conditions [29], especially for large pitching amplitude, which plays a key role in the second-order effect and the viscous-inviscid interaction for real foils in real fluids [30].

The studies on the sinusoidally pitching foil are summarized in Table I. Using flow visualization and laser doppler velocimetry (LDV), Koochesfahani [31] estimated the thrust by calculating the momentum deficit from the wake velocity profile. Rueger and Gregorek [32] measured the surface pressure on a pitching NACA 0021 foil and studied the effect of the parameters of the pitching motion. In that study, the amplitude of the sinusoidal motion was limited to 10°. Bohl and

TABLE I. Previous experimental studies on the sinusoidally pitching foil in chronological order.

References	Fluid medium	Experimental technique	Major Re	max (α_m)	k
Koochesfahani [31]	Water	Flow visualization, LDV	12000	4°	0.84–10
Rueger and Gregorek [32]	Air	Surface pressure taps	1.2×10^6	10°	0–0.03
Bohl and Koochesfahani [33]	Water	MTV	12600	2°	4.1–11.5
Schnipper *et al.* [34]	Water	Soap film visualization	1320, 2640	10.5°	0.09–5.65
Mackowski and Williamson [35]	Water	Force sensor, PIV	1.7×10^4	32°	0–12
Andersen *et al.* [36]	Water	Soap film visualization	1320, 2640	10.5°	0.09–5.65
Cordes *et al.* [29]	Air	Surface pressure taps	1.2×10^5	6°	0.025–0.3
Present paper	Water	Force and moment sensors, PIV	$0.59–2.4 \times 10^5$	34°	0.16–2.51

Koochesfahani [33] measured the unsteady wake of a pitching foil by utilizing molecular tagging velocimetry (MTV) and improved the estimation of the mean thrust by taking into account the effect of unsteady velocity fluctuations. Mackowski and Williamson [35] directly measured the forces acting on a pitching aerofoil, and commented on the Reynolds number dependence of the reduced frequency corresponding to the drag-thrust crossover. The drag-thrust crossover marks the transition of the mean streamwise force from drag to thrust with increasing reduced frequency k. The nondimensional parameter is defined as $k = \pi f C/U = \omega C/2U$, where f is the frequency of the oscillation, $\omega = 2\pi f$ is the angular frequency, C is the chord of the foil, and U is the mean freestream velocity. By visualization in a soap film tunnel, Schnipper *et al.* [34] and Andersen *et al.* [36] mapped out wake patterns in a phase diagram with foil-thickness-based Strouhal number against dimensionless amplitude, verified the pitch-amplitude-based Strouhal number as a single value parameter to characterize the transition to the reverse von Kármán vortex street (RvKVS), and further discussed the drag-thrust crossover in relation to the reverse von Kármán vortex street. Cordes *et al.* [29] investigated the applicability of Theodorsen's model for the lift response to a sinusoidally pitching foil by measuring the pressure difference on the aerofoil leading edge instead of directly measuring the lift. They found the mean α to have a larger impact on the lift magnitude response than α_m. However, the study was limited to α_m within 6°.

Previous experimental studies on the applicability of linear inviscid theory have been limited in the range of flow conditions, in particular Reynolds number and α amplitude. Also, the role of the vortex shedding, e.g., LEV and RvKVS, on the dynamic force and moment response to the pitching motion has not been described clearly. Thus, to date, a number of questions with respect to sinusoidally pitching foil motion remain unclear. The present paper focuses on the following questions.

(1) Can we identify and characterize different regimes of vortex shedding? (See Sec. III A.)

(2) How do the parameters α_m, k, and Re affect the dynamic force and moment responses beyond the linear inviscid theory? (See Sec. III B.)

(3) What are the effects of the vortex shedding regimes on the dynamic responses? (See Sec. III C.)

To tackle the above issues, we experimentally studied the unsteady hydrodynamics of a sinusoidally pitching NACA 0012 hydrofoil with chord Reynolds number ranging from 5.9×10^4 to 2.4×10^5. This extends the upper limit of the Reynolds number range reported in literature for pitching hydrofoils. The parameter space of hydrofoil kinematics is spanned by reduced frequency up to 2.51 and pitching amplitude up to 34°. The dynamic forces including lift, drag, and moment are directly measured by means of load balance and torque sensor. Phase-locked PIV is used to measure the flowfields.

II. EXPERIMENTAL SETUP

The experiments were conducted in a large-scale recirculating water channel at Shanghai Jiao Tong University, which provides a uniform freestream inflow velocity with the nominal turbulence level less than 2%. The test section is 3 m wide and 1.6 m deep. A rigid NACA 0012 hydrofoil with a uniform chord length of $C = 0.2$ m and a span of $S = 0.8$ m was fully submerged in water. The mid-span plane of the hydrofoil was basically aligned with the mid-depth plane of the test section. On the side rails of the test section an inverted trapezoidal steel frame was attached to support the hydrofoil as well as the force and moment sensors and the motion mechanism as shown in Figs. 1(a) and 1(b). The hydrofoil was made of an aluminum alloy with the surface polished and flat-black spray-painted. The hydrofoil performed sinusoidal pitch oscillation $\alpha = \alpha_m \sin 2\pi f t$ with the independently adjusted oscillation amplitude α_m and frequency f [see Fig. 1(c)]. The blockage ratio of the pitching hydrofoil in the test section is 1.9% when the hydrofoil pitches at the maximum angle of attack ($\alpha = 34°$). A solid, round shaft was fixed to the foil at quarter chord ($C/4$ from the leading edge), passing through but not touching a fairing to transmit force to a load balance. The fairing had the shape of a NACA 0030 profile and extended from the location 1 cm above the upper

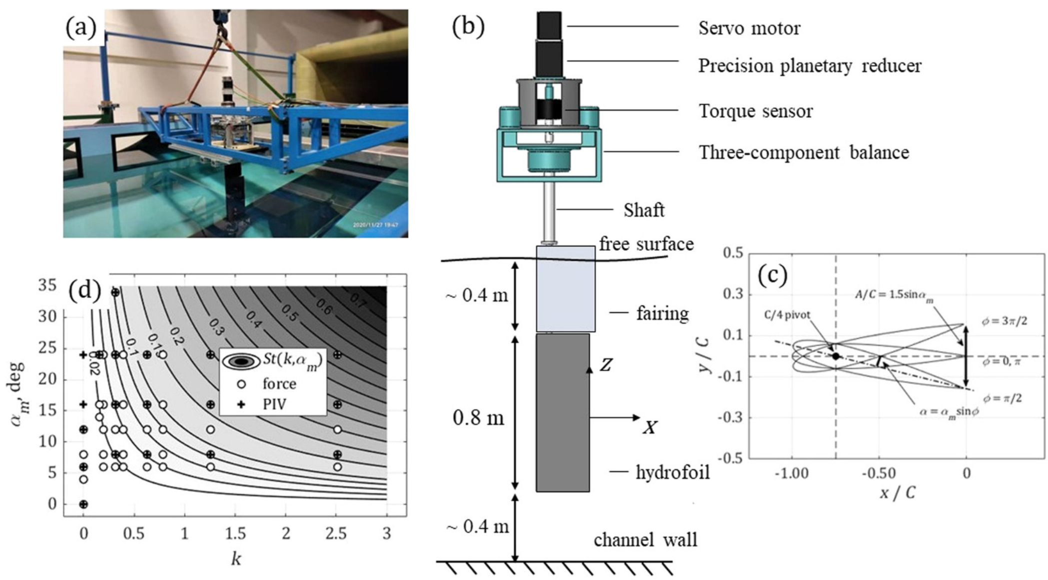

FIG. 1. (a) Picture of the experimental setup. (b) Schematic of the vertically mounted hydrofoil with the servo motion system and force measuring sensors. (c) Schematic of the sinusoidally pitching hydrofoil in spanwise view. (d) Force measurements (circle) and PIV measurements (cross) marked in the $k - \alpha_m$ phase diagram with St-contour lines.

tip of the hydrofoil to the location 5 cm above the free surface. The shaft end was connected to a torque sensor to measure the pitching moment. The shaft's rotation was monitored by an incremental encoder. Although no end plate was used in the present large-scale experiment to avoid undesired mechanical effects, the fairing suppressed the tip effect at the upper end. The three-dimensional effect due to the lack of end plates was negligible on the quasi-two-dimensional flowfields on the mid-span plane of the hydrofoil [35]. The similar statistics of force coefficients when compared to the nominally two-dimensional results of Mackowski and Williamson [35], including the variance of the lift coefficients and the phase lag of lift and drag [discussed later; see Fig. 7(a) and Figs. 9(a) and 9(b), respectively], indicate that the three-dimensional effect on the force measurements is very limited [37,38]. The coordinate system was defined with its origin located at the trailing edge of the hydrofoil at zero α. The positive x axis was oriented downstream, the y axis indicated the transverse direction, and the positive z axis extended vertically upwards along the span of the hydrofoil [see Figs. 1(b) and 1(c)].

Experiments were conducted at freestream velocities $U = 0.25, 0.5, 0.8,$ and 1.0 m/s, resulting in chord-based Reynolds numbers of $\mathrm{Re} = UC/\nu = 5.9 \times 10^4, 1.2 \times 10^5, 1.9 \times 10^5,$ and 2.4×10^5, where ν is the kinematic viscosity of water. The oscillating frequencies and the pitching amplitudes were set as $f = 0.25, 0.5,$ and 1.0 Hz and $\alpha_m = 6^\circ, 8^\circ, 12^\circ, 14^\circ, 16^\circ, 24^\circ,$ and 34°, respectively. This resulted in reduced frequencies in the range of $0.16 \leqslant k \leqslant 2.51$. When varying k by varying U (and therefore Re) the comparatively weak effect of Re allows for qualitative discussion of the influence of k on the shedding regimes, which are primarily determined by k and α_m as discussed below in Sec. III A. In turn, in order to separate the weak Re effect from the strong k effect (discussed below in Sec. III B) cases with different Re but equal k need to be compared. This requires the dimensionless parameter space to include various samples with the identical k but different U and f. The amplitude-based Strouhal number $\mathrm{St} = fA/U = (1.5k \sin \alpha_m)/\pi$, where A is the total excursion of the hydrofoil trailing edge, is introduced combining k and α_m into a single parameter useful for characterizing the wake pattern [34]. Its values were in the range of $0.010 \leqslant \mathrm{St} \leqslant 0.488$. The basic experimental parameters of PIV measurements and force measurements for the pitching hydrofoil are summarized in Appendix A and marked in the $k - \alpha_m$ phase diagram with the St-contour lines in Fig. 1(d). Measurements for the stationary hydrofoil were also performed. The boundary layers over the hydrofoil in the present Re range undergo transition to the turbulent state, which was assessed by comparing the measured drag coefficient and thickness of the boundary layer with the theoretical values of laminar and turbulent boundary layers.

The load balance was used to measure the lift and drag by transforming three full bridge strain gauges with temperature compensation. The comprehensive accuracy of the gauges with 95% confidence factor are within ±0.16, ±0.47, and ± 0.46% of individual full scales (200, 100, and 100 N). The torque sensor was used to measure the moment independently, with the comprehensive accuracy (95% confidence) less than ±0.12% full scale (10 N m). The resulting relative errors of lift, drag, and moment due to the measurement uncertainty were estimated. The maximum values were, respectively, 0.7, 3.4, and 1.6% of the peak-peak values of corresponding variations in one pitching cycle. Pre- and postcalibrations were carried out for the load balance and the torque sensor, showing little drift. In the calibrated transformation matrix of the balance, nonprincipal coefficients related to the cross-talk effect were less than 1% of the principal coefficients that determined the lift and drag results. Resulting from linear regression of the calibrated data, the squares of the correlation coefficients were very close to 1, indicating a very good linear response of the balance and the torque sensor over the expected range of the measurement. The time series of lift, drag, and moment were acquired simultaneously with the angular speed of the servo motor. The sampling rate and low-pass cutoff frequency were set at 200 and 30 Hz, respectively. Thirty oscillation periods were recorded including the startup transients. Before each set of experiments, the zero-pitch position was carefully reset by adjusting the pitch angle such that no lift was measured. Measurements were also performed without water to obtain the forces due to the foil inertia, which were subtracted from the force measurements with the foil in water to provide the hydrodynamic force only. After measuring the lift L, the drag D, and the moment M, the corresponding coefficients were computed as, respectively, $C_l = 2L/(\rho U^2 CS)$, $C_d = 2D/(\rho U^2 CS)$, and $C_m = 2M/(\rho U^2 C^2 S)$, where ρ is the density of water.

For PIV measurements, the flow was seeded with hollow glass spheres (diameter 55 μm). The seeding density was approximately 0.03 particles per pixel. A Nd-YAG pulsed laser illuminated the flowfield in the mid-span plane of the foil. A mirror reflected the light back to the flowfield on the opposite side of the model to partially allow for measurements on both sides of the foil. Light sheet thickness in the field of view was approximately 2 mm. Two CCD cameras (14 bit, sensor size 4008×2672 pixels, pixel pitch 9.0 μm) with Nikon AF NIKKOR objectives (focal length 40 mm, operated at f-stop 4) were mounted next to each other in a streamwise arrangement to capture a large planar field of view. The distance between the sensor plane and the measurement plane was approximately 1 m resulting in an optical magnification of 0.045. The time separation between a pair of laser pulses was adjusted to ensure a particle shift less than 8 pixels for different freestream velocities. Collection and analysis of PIV images were carried out using the LaVision DaVis software package. The two cameras were calibrated by using the pinhole camera model, providing the stitching of velocity fields. Triggered by a signal from the servo controller, the laser pulses and camera exposures were locked with respect to the pitching phase ϕ of the hydrofoil. Flowfields were recorded for 20 pitch periods (including the startup period). Before vector calculation, the sliding background subtraction was used to relieve the local intensity fluctuation in the image background due to reflection. After correction to image distortion due to perspective projection and camera lens errors, images were interrogated with an iterative multipass cross-correlation method. The initial correlation step was processed with interrogation windows of size 64×64 pixels and 50% overlap. Two refinement passes resulted in a final interrogation window size of 32×32 pixels with 75% overlap. High accuracy mode of image correction with Lanczos filter was applied for the final passes of correlation calculation. Outliers in the computed velocity data were detected (correlation peak ratio less than 1.1) and replaced by reinterpolation with a median filter of 3×3. The outliers were usually found near the pitching hydrofoil (due to reflection, loss of correlation, velocity shear) and their number in the high-frequency cases was about 6% of the total number of vectors in the field. The resulting spatial resolution of the measurement was 1.65×1.65 mm^2, and the pitch was less than 0.83% of the chord length. The particle image diameter was estimated to be approximately 3 pixels, for which the root-mean-square random error of the present cross-correlation is no greater than 0.5% of the freestream velocity [39].

III. RESULTS AND DISCUSSION

A. Regimes of vortex shedding

In order to identify the different regimes of vortex shedding in the high Re unsteady hydrodynamics with the pivot located at $C/4$ and to answer question 1 raised in the introduction, this section describes the flow structure under various flow conditions of reduced frequency k and pitching amplitude α_m. In comparison to k and α_m the Reynolds number affects the vortex pattern less over the present Re range. In the following, ϕ is used to denote the phase of pitch oscillation ($\alpha = \alpha_m \sin\phi$). The phase-averaged vorticity fields, obtained by phase-averaging the last 19 vorticity fields of the 20 records, reveal the vortical structures in the flowfields. The first visualization was not used to exclude the transient startup period. The statistical uncertainty of the phase-averaged vorticity in the wake is no larger than 3.6% of the peak-peak value of the corresponding field (95% confidence) [40]. The statistical uncertainty inside the boundary layer is large in comparison (less than 23.2%). Furthermore, the geometric features and dynamic convection properties of different flow patterns are discussed by identifying and characterizing the structure in the wake.

1. Trailing-edge vortex shedding

Figure 2 shows filled contours of the phase-averaged and normalized vorticity field $\langle\omega\rangle C/U$ for $k = 0.63, 1.26,$ and 2.51 with fixed $\alpha_m = 16^\circ$ and for different pitching phases ϕ, where different levels of vorticity are indicted by different color levels. The phases $\phi = \pi/4$ and $\pi/2$ correspond to the hydrofoil pitching up to extreme α, and $\phi = \pi$ and $5\pi/4$ correspond to pitching past zero α with increasing α. The flow appears to be attached in all cases, but the wake structure differs significantly when k increases from 0.63 to 2.51, which is discussed below.

For $k = 0.63$ (Fig. 2, left column), the boundary layer vorticity originating from two sides of the oscillating hydrofoil alternately sheds off from the trailing edge and initially drifts towards the opposite side of the wake while convecting downstream. The wake is characterized by continuous, undulating vorticity sheets with limited curvature. This pattern is hence referred to as undulating wake (UW). In the UW pattern, no discrete vortices with concentrations of vorticity or other vortex indicators, such as Q, λ_2, λ_{ci}, and R criteria [41–44], can be discerned from instantaneous visualizations or from phase-averaged flowfields. This observation differs from that of Koochesfahani [31] with the UW carrying the naturally shedding von Kármán vortices. The present UW pattern is also very different from the complicated pattern of $4P + 2S$, $6P + 2S$, and $8P$, etc., shedding per oscillation period (where P refers to a pair of vortices and S refers to one discrete vortex), as observed by Schnipper *et al.* [34] and Andersen *et al.* [36] in the same reduced frequency range of $k \leqslant 0.63$. It is noted that the chord Reynolds numbers in these previous studies are one or two orders of magnitude smaller than the present one (see Table I). Although the Re effect on the wake patterns is not obvious in the present high Re range, the comparison with low Re studies reveals that the smaller Re the more complicated the vortex pattern in the wake for low k. For the weakly unsteady wake at low k, the increased inertial effect relative to the viscous effect at high Re is detrimental to the formation of concentrated vortex structures with strong coherence. Hence, the UW pattern instead of a vortex pattern is observed.

At $k = 1.26$ (Fig. 2, middle column), vorticity produced in the boundary layer sheds from the trailing edge and rolls up into an array of compact, discrete vortices of opposite rotation. In this vortex array, the vortex with positive vorticity locates above the transverse centerline, while the one with negative vorticity locates below the centerline. The transverse alignment is reversed compared

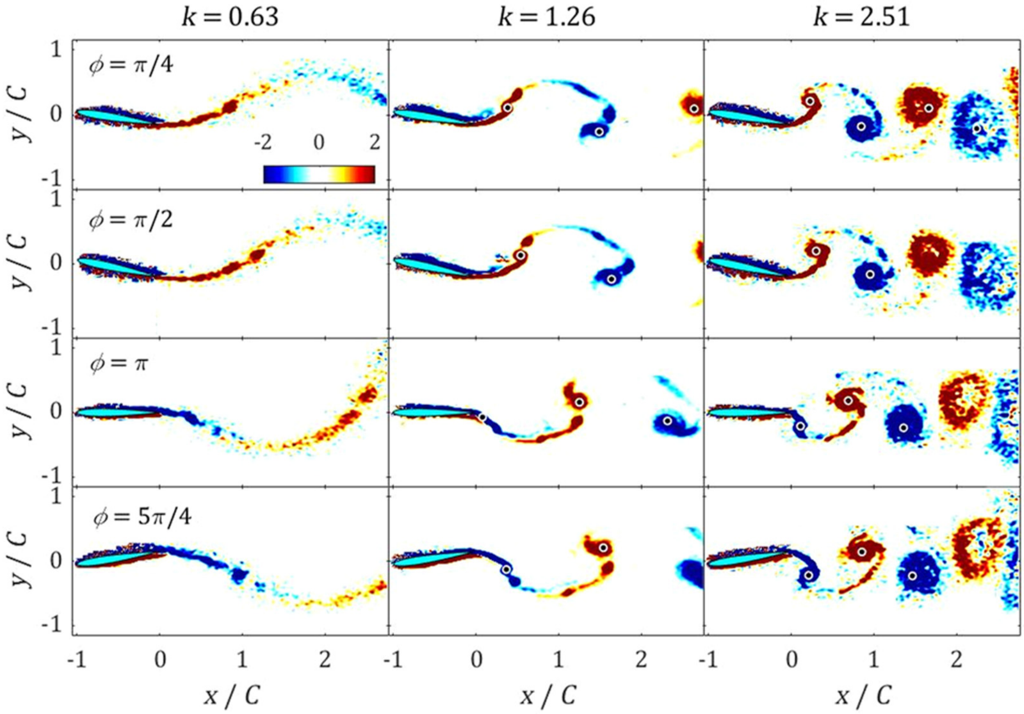

FIG. 2. Nondimensional vorticity distribution $\langle\omega\rangle C/U$ of the pitching hydrofoil for $k = 0.63, 1.26, 2.51$ with $\alpha_m = 16^\circ$ and $\phi = \pi/4, \pi/2, \pi, 5\pi/4$. Re $= 5.9 \times 10^4, 1.2 \times 10^5, 5.9 \times 10^4$ for columns from left to right. The vortex cores are marked by filled circles.

with the von Kármán vortex street behind a cylinder, hence it is termed as the reverse von Kármán vortex street [13,34,35]. At even higher $k = 2.51$ (Fig. 2, right column), the wake pattern of the RvKVS persists but with a smaller streamwise distance between positive and negative vortex cores, which are, respectively, defined as the local maximum and minimum vorticity in a discrete vortex. The locations of identified vortex cores are marked by filled circles in the phase-averaged vorticity fields. Different from undulating vorticity sheets of the UW pattern, discrete vortices of the RvKVS pattern have very large curvature near the vortex cores. The RvKVS in Fig. 2 qualitatively agrees with the results of Koochesfahani [31], Bohl and Koochesfahani [33], Schnipper *et al.* [34], and Andersen *et al.* [36]. For all cases of the RvKVS pattern, a pair of opposite vortices is shed off from the sharp trailing edge of the hydrofoil per oscillation period. Hence, the frequency of the RvKVS pattern is nearly locked with the oscillation frequency of the hydrofoil.

Figure 3 shows the nondimensional vorticity at $\phi = \pi$ for three different pitching amplitudes α_m and for the same reduced frequencies as shown in Fig. 2. In each column of Fig. 3 (fixed k), when α_m increases, the wake pattern remains similar with quantitative differences only. For the UW pattern ($k = 0.63$) the curvature of the undulating vorticity sheet increases with α_m. When α_m increases up to 24°, although a discontinuity is observed in the slope of the undulating vorticity sheet, the curvature is not large enough to form discrete vortices with vorticity concentration. The transition from the UW pattern to the RvKVS pattern may occur with a further increase of α_m. For the RvKVS pattern ($k = 1.26$ or 2.51), the main difference is that both the transverse distance between a pair of opposite vortex cores and the size of vortices increase with α_m. In the case of the RvKVS with $k = 2.51$ and $\alpha_m = 24^\circ$ the second pair of alternating vortices interacts and dissipates vorticity at $x/C > 2$ due to the increasing vortex size with α_m. The phenomenon of vorticity dissipation within the RvKVS pattern was also found in the studies of Koochesfahani [31] (Re $= 1.2 \times 10^4$)

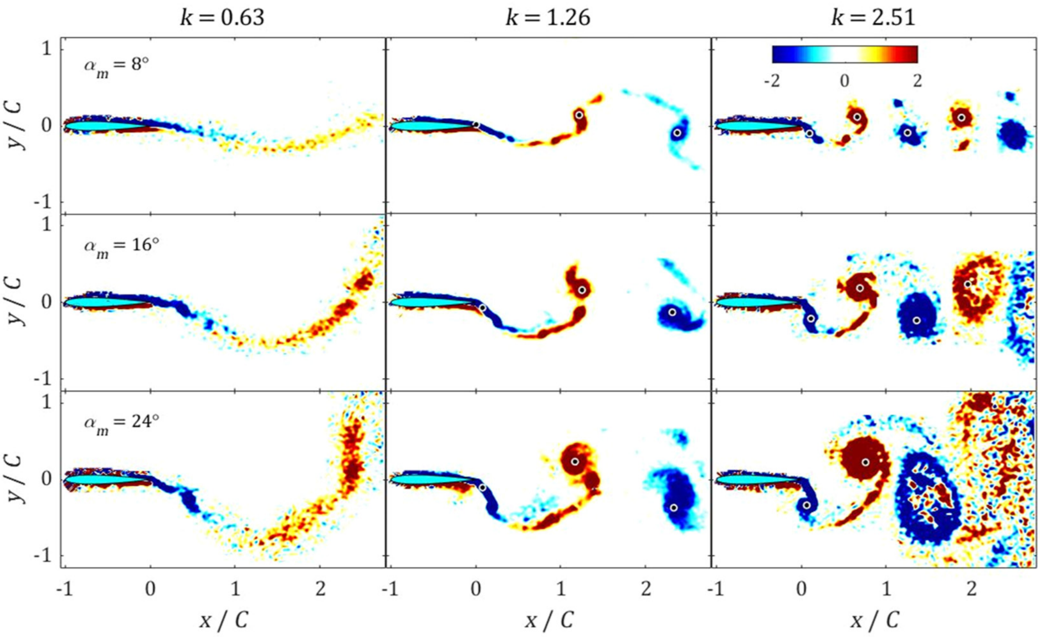

FIG. 3. Nondimensional vorticity distribution $\langle\omega\rangle C/U$ of the pitching hydrofoil for $\alpha_m = 8^\circ, 16^\circ, 24^\circ$ with $k = 0.63, 1.26, 2.51$ and $\phi = \pi$. Re $= 5.9 \times 10^4, 1.2 \times 10^5, 5.9 \times 10^4$ for columns from left to right. The vortex cores are marked by filled circles.

and Schnipper *et al.* [34] (Re = 1320 and 2640), but at farther downstream locations ($x/C > 3$ and 10, respectively). Based on these observations, the streamwise location of interaction and dissipation is found to be subject to α_m and Re. On one hand, the vortex size increases with α_m. Once the size approaches to the spacing between two adjacent vortex cores which is determined by k (see Fig. 3 and Table II), the interaction between opposite vortices leaves a blurred wake without clear vortex structures [34]. On the other hand, the present wakes are in a turbulent state with high Re, while

TABLE II. Basic properties of three shedding regimes.

Wake pattern	k	α_m	St	λ_x/C	κ_m	D_y/C	U_c/U
Undulating wake	0.31	8°	0.021	4.10	0.20		0.84
	0.31	16°	0.041	4.19	1.11		0.74
	0.63	8°	0.042	3.65	1.04		0.97
	0.63	16°	0.083	3.71	1.60		0.78
	0.63	24°	0.122	3.74	2.21		0.71
	0.16	24°	0.031	10.0		<-0.27	0.60
Leading-edge vortex	0.31	24°	0.061	7.07		-0.12	0.71
	0.31	34°	0.084	6.40		<-0.19	0.61
	1.26	8°	0.084	2.32		0.19	0.80
	1.26	16°	0.165	2.27		0.33	0.97
Reverse von Kármán	1.26	24°	0.244	2.40		0.62	0.98
vortex street	2.51	8°	0.167	1.15		0.22	0.82
	2.51	16°	0.331	1.25		0.38	1.05
	2.51	24°	0.488	1.42		0.52	1.27

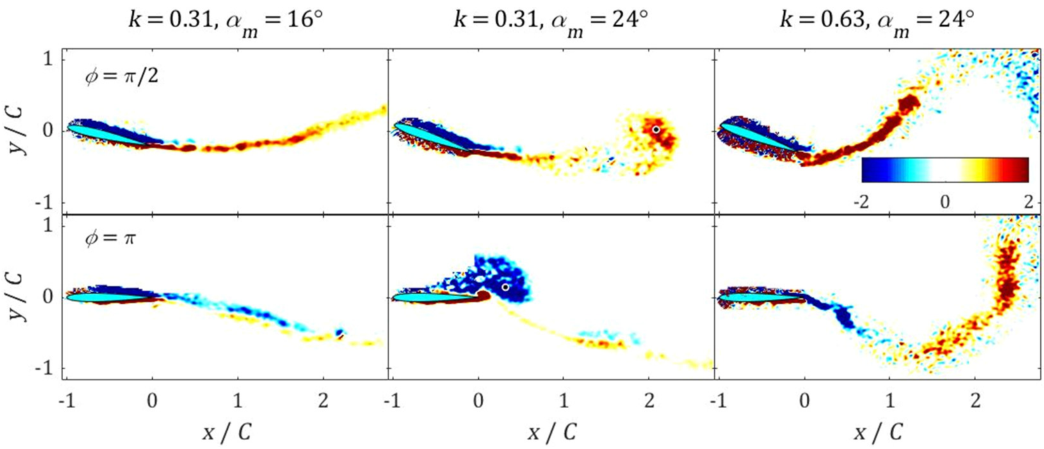

FIG. 4. Nondimensional vorticity distribution $\langle\omega\rangle C/U$ of the pitching hydrofoil for $k = 0.31$ and $\alpha_m = 24°$ with $\phi = \pi/2, \pi$. Re $= 1.2 \times 10^5$, 1.2×10^5, 5.9×10^4 for columns from left to right. The vortex cores are marked by filled circles.

the soap visualizations by Schnipper *et al.* [34] focus on laminar wakes with low Re. The discrete vortices in the turbulent wake are less likely to remain coherent while convecting downstream. Hence, the vorticity dissipation is observed closer to the hydrofoil when compared to the lower Re results.

2. Leading-edge vortex shedding

Figure 4 shows the vorticity fields $\langle\omega\rangle C/U$ at $\phi = \pi/2$ (top) and $\phi = \pi$ (bottom) for $k = 0.31$ and $\alpha_m = 24°$. The subplots correspond to the parameter combinations of $k = 0.31$, $\alpha_m = 16°$ (left), $k = 0.31$, $\alpha_m = 24°$ (middle), and $k = 0.63$, $\alpha_m = 24°$ (right). The case of $k = 0.31$ and $\alpha_m = 24°$ deserves attention since two alternating LEVs, which form and shed off upstream of the trailing edge, are captured in the wake at $\phi = \pi/2$ and π, respectively. When approaching zero α (Fig. 4, middle column, bottom row) during pitch, the flow separates from the upper surface of the hydrofoil, leading to the formation of a negative-vorticity LEV. With further flow separation, the LEV sheds off from the upper surface and is convected past the trailing edge. During this phase, the flow remains attached on the lower surface. The shedding of the LEV from the hydrofoil induces the recovery of the attached flow condition as well as the disappearance of the low-pressure region on the upper surface, the location of which can be approximated by the core of the LEV according to Jeong and Hussain [42]. When the LEV is convected further downstream, the attached flow condition completely recovers. In contrast, in the UW and RvKVS patterns, no such drastically thickened vorticity layer as in the LEV pattern is found on the sides of the hydrofoil. Thin vorticity layers are found always attached on the sides with vorticity only shedding off from the trailing edge during the hydrofoil pitching. In addition, one significant difference between LEV and RvKVS can be observed: the negative-vorticity LEV (clockwise vortex with negative vorticity) in the wake locates at positive transverse position ($y/C > 0$), while the positive-vorticity LEV (counterclockwise vortex with positive vorticity) locates at $y/C < 0$. The transverse arrangement of positive-vorticity and negative-vorticity LEVs is inverted with respect to the RvKVS pattern. Note that although this LEV pattern exhibits some features of the vKVS pattern it is different from the vKVS patterns observed by Bohl and Koochesfahani [33] and Schnipper *et al.* [34] that originate from the trailing edge.

Two necessary conditions for the formation of the LEV can be derived from Fig. 4: large pitching amplitude and low reduced frequency (e.g., $\alpha_m > 16°$ and $k < 0.63$). With smaller α_m or larger k the wake pattern changes to UW. These two conditions for the LEV pattern were also presented in the phase plane representation of wake patterns by Anderson *et al.* [13]. Figure 5 shows the

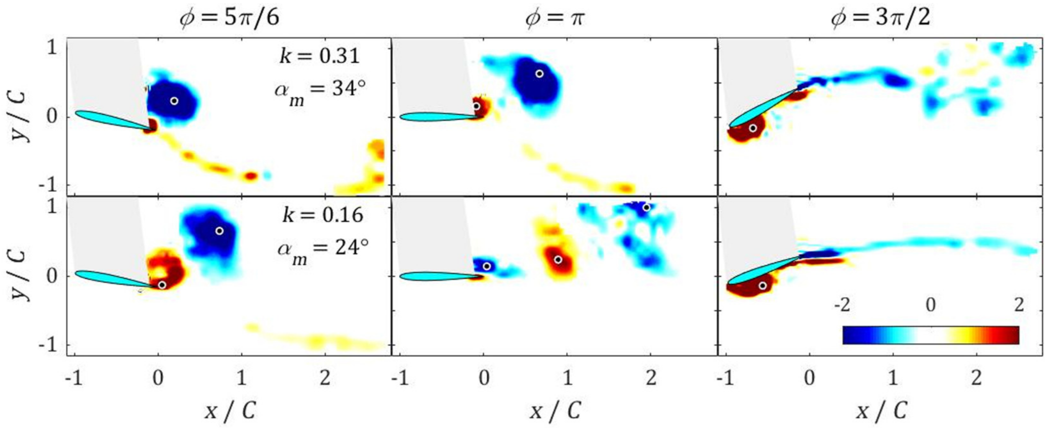

FIG. 5. Nondimensional vorticity distribution $\langle\omega\rangle C/U$ of the pitching hydrofoil for $k = 0.31, \alpha_m = 34^\circ$, $\mathrm{Re} = 1.2 \times 10^5$ and $k = 0.16, \alpha_m = 24^\circ$, $\mathrm{Re} = 2.4 \times 10^5$ with $\phi = 5\pi/6, \pi, 3\pi/2$. The vortex cores are marked by filled circles. Gray regions indicate laser sheets blocked by the hydrofoil.

phase-averaged vorticity fields at $\phi = 5\pi/6, \pi,$ and $3\pi/2$ for $k = 0.31, \alpha_m = 34^\circ$ (top) and $k = 0.16, \alpha_m = 24^\circ$ (bottom). In these two cases, when the hydrofoil is pitching from the maximum α to zero α, a similar period of the negative-vorticity LEV is observed as in the case of $k = 0.31, \alpha_m = 24^\circ$ (Fig. 4, middle column). The negative-vorticity LEV sheds from the upper surface, passes by the trailing edge, and convects in the wake. At $\alpha = -\alpha_m$ ($\phi = 3\pi/2$), a positive-vorticity LEV is observed to form on the lower surface. Both the cases with larger α_m and with smaller k are subject to the LEV regime, which gives further support to the necessary conditions. In addition, during the pitching phase from $\phi = \pi/2$ to π, only one negative LEV as in the case of $k = 0.31, \alpha_m = 24^\circ$ but also additional trailing-edge-shedding vortices are observed in Fig. 5. In the case of $k = 0.31, \alpha_m = 34^\circ$, a positive-vorticity vortex is observed to shed from the trailing edge at $\phi = \pi$. In the case of $k = 0.16, \alpha_m = 24^\circ$, the positive-vorticity vortex is observed at $\phi = 5\pi/6$, and another negative-vorticity vortex is observed to shed at $\phi = \pi$.

3. Statistical features of vortex shedding

This section quantifies the geometric features and the convection velocity U_c for the UW, RvKVS, and LEV regimes. For the RvKVS pattern, the streamwise wavelength λ_x is defined as the streamwise distance between two adjacent vortex cores of identical rotation. D_y is the difference in the y coordinate between two adjacent cores of counter-rotating vortices (y of the positive vorticity peak minus the y of the negative one). The values of λ_x and D_y in the RvKVS case are basically constant in the present streamwise range, thus the mean values are obtained by averaging the corresponding distances of vortex pairs at different x and at varied ϕ. Note that the vortices, which are observed to interact and dissipate, are not considered to quantify the geometric features.

In the LEV regime, characterization of λ_x and D_y is only performed for the leading-edge vortices rather than the accompanying trailing-edge vortices. Due to the limited streamwise extent of the field of view in the PIV experiments, λ_x and D_y of the long-wavelength LEV pattern are obtained from vorticity fields at several phases (e.g., $\phi = \pi/2$ and π). By considering the symmetry of the hydrofoil motion and the vorticity fields, $\lambda_x/4$ of the LEV pattern is estimated as the streamwise distance between the positive vortex core at $\phi = \pi/2$ and the negative vortex core at $\phi = \pi$, based on the frequency-lock relation between the hydrofoil motion and the vorticity fields [which is shown later by $U_c/\lambda_x f \approx 1$ for LEV in Fig. 6(b)]. D_y of opposite LEVs is found to be basically unchanged in the case of $k = 0.31, \alpha_m = 24^\circ$. However, in the cases of larger α_m and smaller k, D_y is found to vary when LEVs are convected downstream, thus the value range instead of the mean value is given.

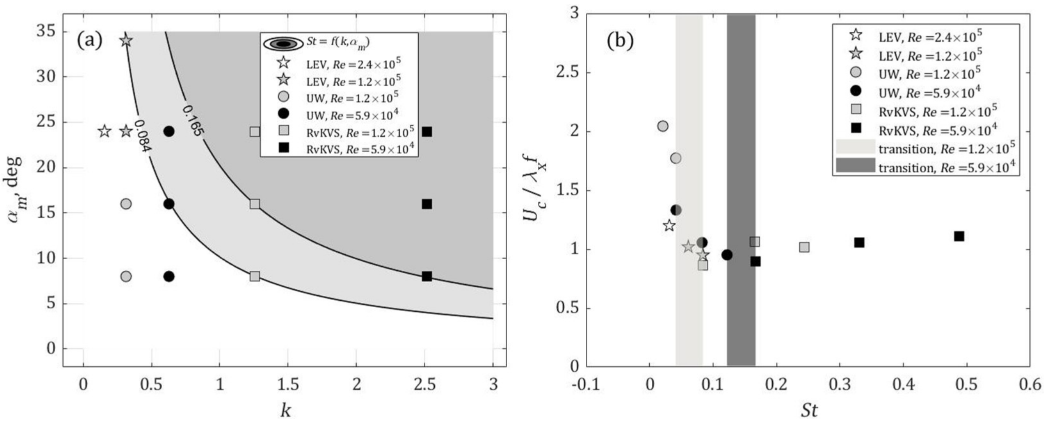

FIG. 6. (a) Parameter regions dominated by three wake patterns on the $k - \alpha_m$ plane with St-contour lines. (b) Nondimensional characteristic frequency $U_c/\lambda_x f$ vs St, and transition region from UW to RvKVS. LEV, UW, and RvKVS are, respectively, marked by pentagram, circle, and square, in white, gray, and black for $\mathrm{Re} = 2.4 \times 10^5$, 1.2×10^5, 5.9×10^4. Gray level of transition band decreases with Re.

To obtain the characteristic convection velocity U_c of the vortex core for the RvKVS and LEV, Taylor's frozen-turbulence hypothesis is applied and the temporal-spatial course of the discrete vortex core is tracked for varied ϕ. Because the UW does not feature discrete vortices, the ridge of the UW pattern is extracted and the highest and the lowest transverse positions are identified to quantitatively characterize λ_x, U_c, as well as the maximum curvature κ_m. The streamwise positions of ridge peaks and ridge troughs for UW patterns and the streamwise positions of vortex cores for LEV and RvKVS patterns are found to be basically linear with time, implying stable vorticity convection over the measurement domain. Hence, a first-order polynomial fit is used to quantify U_c.

Table II lists relevant parameters for the three shedding regimes. For all patterns except LEV, λ_x/C varies little with α_m, and is mainly determined by k. λ_x/C monotonically decreases with k within $0.31 \leqslant k \leqslant 2.51$, and this trend was also observed within $5.2 \leqslant k \leqslant 11.5$ by Bohl and Koochesfahani [33], albeit with a less drastic decrease for low k. D_y/C of RvKVS is positive and nearly proportional to $\sin\alpha_m$, but does not change much for $k = 1.26$ and 2.51. The ratio of D_y/C over $\sin\alpha_m$ is about 1.39, thus the ratio of D_y over the total excursion of trailing edge A is about 0.93. This in turn implies that the vortex cores in the RvKVS pattern shed off from the trailing edge when the hydrofoil reaches approximately 93% amplitude, regardless of how fast the hydrofoil pitches, given that the transverse locations of alternating vortices do not change much during the convection in the wake. In contrast, the LEV core begins to form when the hydrofoil pitches from α_m, convects over the suction surface, and then sheds off before the hydrofoil approaches again zero α. When convecting in the wake, the LEVs move away even further from $y = 0$ in the cases of $k = 0.31$, $\alpha_m = 34^\circ$ and $k = 0.16$, $\alpha_m = 24^\circ$. Therefore, the negative-vorticity LEV locates at $y/C > 0$ while the positive-vorticity LEV locates at $y/C < 0$, leading to a negative value of D_y/C. For the UW pattern, the variation of U_c/U with k shows an opposite trend as with α_m. With fixed $k = 0.63$, U_c/U decreases to the minimum level of 0.71 when α_m increases to 24°. The value of U_c/U is found to be larger than the one for the RvKVS with $\mathrm{St} \geqslant 0.33$, implying the transition of the mean velocity profile from a wake-type deficit to a jet-type surplus as observed by Bohl and Koochesfahani [33].

Figure 6 shows the parameter regions dominated by the UW, LEV, and RvKVS patterns on the $k - \alpha_m$ plane and the dependence of the characteristic frequency of the wake $U_c/\lambda_x f$ on the amplitude-based Strouhal number St. Two opposite trends are observed for the UW and RvKVS shedding regimes: for UW, U_c/λ_x monotonically decreases from $2f$ to f, while for RvKVS, U_c/λ_x increases very slowly in the vicinity of f, implying that the characteristic frequency of the RvKVS is approximately locked to the pitching frequency. St serves as a single-value parameter to indicate the boundary between the UW and RvKVS regimes at a given Re. In the present paper, a region of transition from the UW to the RvKVS regime is found at $0.041 < \mathrm{St} < 0.084$ for $\mathrm{Re} = 1.2 \times 10^5$, and at $0.122 < \mathrm{St} < 0.167$ for $\mathrm{Re} = 5.9 \times 10^4$. In the low Re study by Schnipper *et al.* [34], the transition was found at $\mathrm{St} = 0.18$ for $\mathrm{Re} = 1320$ and 2640. Based on the available results, the transition St shows a decreasing trend with increasing Re. At $\mathrm{Re} = 1.2 \times 10^5$, two parameter points in the LEV regime are found in the transition region from UW to RvKVS, implying that St appears not sufficient to identify the LEV pattern. However, combined with Re, St characterizes well the distribution of UW and RvKVS regimes in the parameter space.

B. Force and moment responses

This section describes the statistical behavior and the phase response of the dynamic force and moment coefficients C_l, C_d, and C_m in order to discuss the effects of the reduced frequency k, the amplitude α_m, and the chord Reynolds number $\mathrm{Re} = UC/\nu$. Linear inviscid theoretical models, i.e., Theodorsen's model [5], Garrick's model [8], and Fernandez-Feria's model [20], for the purely pitching hydrofoil with the $C/4$ pivot are derived in Appendix B. Note that the theoretical predictions only consider the variation of reduced frequency k with the assumption of small α_m and infinite Re. In comparison, the measured statistical results reveal the nonlinear effect of large α_m and the viscous effect of low Re at low k, while the measured phase lags of force and moment coefficients with respect to the hydrofoil pitch manifest α_m-dependent features, which addresses question 2 raised in the introduction.

1. Statistical behavior

The measured mean and standard deviation are denoted by an overline and σ, respectively, for C_l, C_d, and C_m. Because the hydrofoil is symmetric about zero α, the mean values $\overline{C_l}$ and $\overline{C_m}$ are approximately zero with very small scatter for varied α_m, k, and Re. In contrast, both $\sigma(C_l)$ and $\sigma(C_m)$ increase with α_m and k, and show a little difference with varying Re at low k.

For low α_m, a linear variation of $\sigma(C_l)$ and $\sigma(C_m)$ with α_m can be observed. This linear relation is consistent with Theodorsen's model. For high α_m, however, the measured data are found to deviate from the linear trend. Figures 7(a) and 7(b) explore the linear relation in terms of $\sigma(C_l)/\alpha_m$ and $\sigma(C_m)/\alpha_m$ for varying k and Re. $\sigma(C_l)/\alpha_m$ of $\alpha_m = 8^\circ$ (pentagram symbol) by Mackowski and Williamson [35] with smaller $\mathrm{Re} = 1.7 \times 10^4$ is plotted for comparison. The solid line indicates the predicted results by Theodorsen's model. The fitted slopes for $\alpha_m \leqslant 12^\circ$ (filled symbols) show a better agreement with the predicted curve than those for larger α_m (hollow symbols), indicating the nonlinear effect of large α_m.

The Re effect at low k is observed in comparison of the measured $\sigma(C_l)/\alpha_m$ and $\sigma(C_m)/\alpha_m$ for $\alpha_m \leqslant 12^\circ$ (filled symbols) with Theodorsen's model. In Figs. 7(a) and 7(b), $\sigma(C_l)/\alpha_m$ and $\sigma(C_m)/\alpha_m$ agree better with the prediction at $k > 1$ than at $k < 1$. In addition, the measured results (filled square and circle) at $k = 0.63$ show larger scatter for different Re values than at $k = 1.26$. As discussed in Sec. III A 1, for relatively weakly unsteady wakes at low k, the wake patterns differ significantly due to varying importance of the viscous effect with Re. According to Theodorsen's model, at low k, the wake-related circulatory component contributes dominantly to the unsteady lift. Hence, the Re effect on wake pattern is reflected in the lift and moment response as the scatter of the measured $\sigma(C_l)/\alpha_m$. To give a rough quantitative estimate of the Re effect, the overall standard deviation from the model is calculated for measured $\sigma(C_l)/\alpha_m$ pertaining to the same Re value. Corresponding to $\mathrm{Re} = 1.7 \times 10^4$, 5.9×10^4, 1.2×10^5, and 1.9×10^5, standard deviations are, respectively, 0.30, 0.26, 0.11, and 0.09. These values are larger than the standard uncertainty of C_l/α_m for varied Re in the present paper ($\leqslant 0.07$). The standard deviation decreases with increasing Re, meaning that $\sigma(C_l)/\alpha_m$ gradually collapses to the prediction with weakening viscous effect.

Different from $\sigma(C_l)$ and $\sigma(C_m)$, $(\overline{C_d} - C_{d0})$ and $\sigma(C_d)$ are proportional to α_m^2 instead of α_m for low pitch amplitude ($\alpha_m \leqslant 12^\circ$). Here, C_{d0} is the viscous, static drag coefficient. Figures 7(c) and 7(d) compare the slopes $(\overline{C_d} - C_{d0})/\alpha_m^2$ and $\sigma(C_d)/\alpha_m^2$ with Garrick's model (dashed line) and

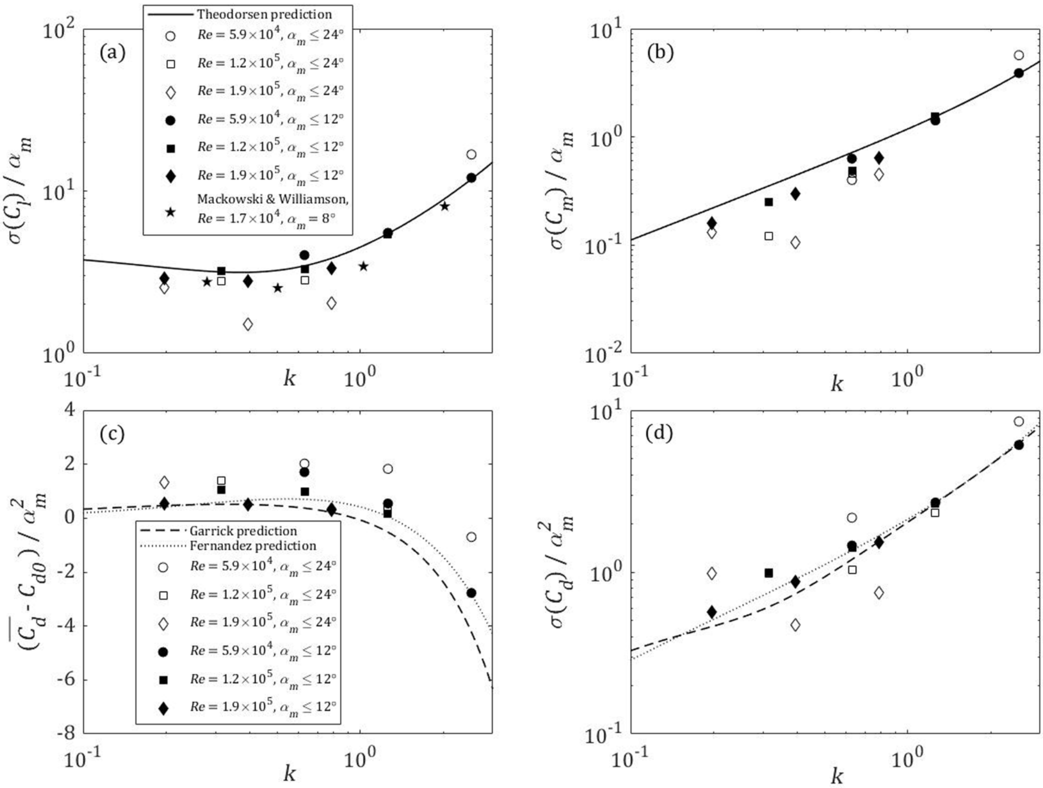

FIG. 7. Measured (a) $\sigma(C_l)/\alpha_m$, (b) $\sigma(C_m)/\alpha_m$, (c) $(\overline{C_d} - C_{d0})/\alpha_m^2$, and (d) $\sigma(C_d)/\alpha_m^2$ vs k for Re $= 5.9 \times 10^4$, 1.2×10^5, 1.9×10^5 (circle, square, and diamond) by linear fitting within $\alpha_m \leqslant 12°$ (filled) and $\alpha_m \leqslant 24°$ (hollow), compared with predictions by Theodorsen [5], Garrick [8], and Fernandez-Feria [20] (solid, dashed, and dotted lines, respectively), and with measured results by Mackowski and Williamson [35] (pentagram).

Fernandez-Feria's model (dotted line). The nonlinear effect of large α_m and the viscous effect of finite Re at low k on the statistics of drag coefficient are observed as for the lift and moment coefficients.

$\overline{C_d}$ is positive except for $k = 2.51$ and St $\geqslant 0.25$ where $\overline{C_d}$ attains a small negative value. This negative $\overline{C_d}$, which corresponds to thrust, is obtained in the parameter region where the RvKVS pattern dominates (see Table II and Fig. 6) and produces a jet-type profile with velocity surplus [33]. The critical k of drag-thrust crossover follows a decreasing trend with Re [35]. It should be noted, however, that the present value is much smaller than predicted by the extrapolation of the $k -$ Re relation provided by Mackowski and Williamson [35] based on a data fit for $1 \times 10^4 <$ Re $< 3 \times 10^4$. The reason for the discrepancy may be that the data for the fitting were restricted to $\alpha_m = 2°$, while in the present case the drag-thrust crossover occurs at $\alpha_m = 12°$. In this sense, to collapse the effect of α_m, the combined parameter St serves better to characterize the drag-thrust crossover. The present crossover is found in the range $0.167 <$ St < 0.250 for Re $= 5.9 \times 10^4$. The St of the drag-thrust crossover is larger than the St of the wake pattern transition from UW to RvKVS ($0.122 <$ St < 0.167 as shown in Fig. 6), because the viscous drag is overcome before thrust is obtained with increasing St.

2. Phase response

The time-dependent coefficients of C_l, C_d, and C_m reveal the dynamic features of the force and moment responses. The time variations can be decomposed into two components, the deterministic

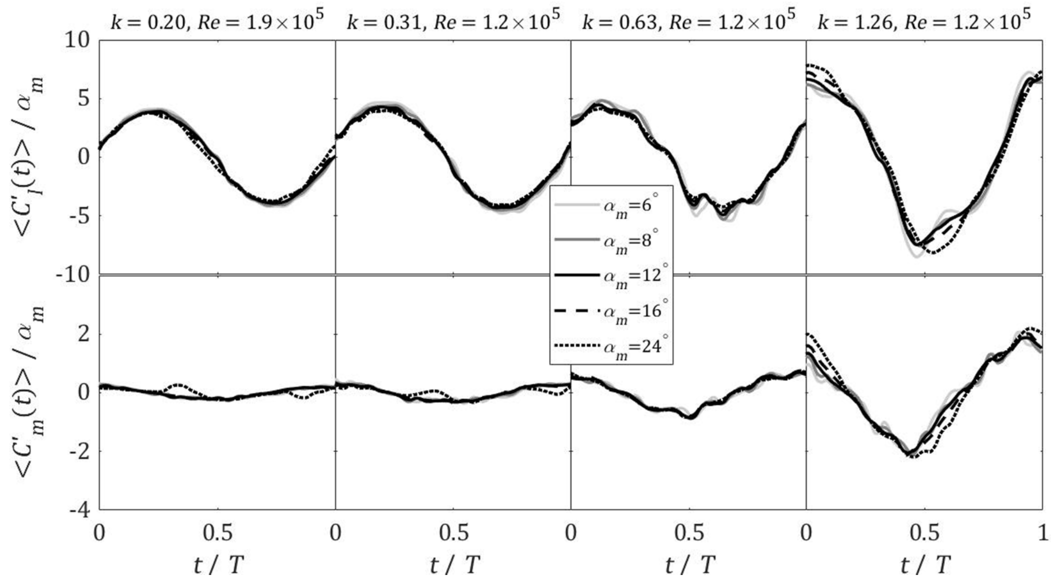

FIG. 8. Phase-averaged C_l' and C_m' normalized with α_m for $k = 0.20, 0.31, 0.63, 1.26$. $\mathrm{Re} = 1.9 \times 10^5, 1.2 \times 10^5, 1.2 \times 10^5, 1.2 \times 10^5$ for columns from left to right. $\alpha_m = 6^\circ, 8^\circ, 12^\circ, 16^\circ, 24^\circ$ indicated by light gray, dark gray, black solid, dashed, and dotted lines, respectively.

component of the response to the hydrofoil pitching (i.e., phase response) and the nondeterministic component due to small-scale turbulence. In order to study the phase response, phase averaging is performed. Because the time series of forces and moment have been acquired simultaneously with the angular speed of the hydrofoil, segments of force and moment coefficients in one cycle of hydrofoil motion $\alpha = \alpha_m \sin 2\pi t/T$ are accurately separated, aligned, and averaged. The startup period is excluded and the total number of averaged segments is 29. The uncertainties of phase-averaged drag, lift, and moment coefficients with 95% confidence factor are, respectively, no larger than 8.3, 3.1, and 6.6% of the peak-peak value of the corresponding variation in one cycle.

The phase-averaged fluctuating lift and moment coefficients C_l' and C_m' are shown in Fig. 8 for varied k and α_m. Normalization with α_m is applied for better comparison. Two notable aspects of the k effect on the time-dependent response are observed. On one hand, the responses of C_l' and C_m' over time agree well for varying α_m, although limited deviation at $k = 1.26$ is observed. On the other hand, C_l' and C_m' show typical sinusoidal behavior at $k = 0.20$ and 0.31. When k increases, the waveforms gradually deviate from the sinusoidal form. The essence of the waveform change is the decoupling between the foil kinematics and force response, resulting from the change in interaction between the foil and the increasingly unsteady flow around [3]. Owing to the inertial effects, a phase difference in which the fluid reaction lags behind the pitching motion is observed. In order to quantitatively estimate the phase lags of C_l, C_d, and C_m with respect to the hydrofoil pitch, cross-correlations and peak identification are conducted. The cross-correlation of α and C_l, C_d, and C_m over multiple cycles effectively suppresses the contribution from the nondeterministic component of small-scale turbulence.

In Fig. 9, measured phase lags ψ_l, ψ_d, and ψ_m for different k, α_m, and Re cases are compared with their theoretical predictions. For ψ_l in Fig. 9(a), the measured results collapse well for varied α_m and Re, and agree well with Theodorsen's model except at $k > 2$, where the measured ψ_l increases to a stable value of 90° but lower than the model prediction (see the hollow circles at $\mathrm{Re} = 5.9 \times 10^4$ and the filled pentagrams by Mackowski and Williamson [35] at $\mathrm{Re} = 1.7 \times 10^4$). For ψ_d in Fig. 9(b), measured values for varied α_m show relatively large scatter. Compared to Garrick's model the trend

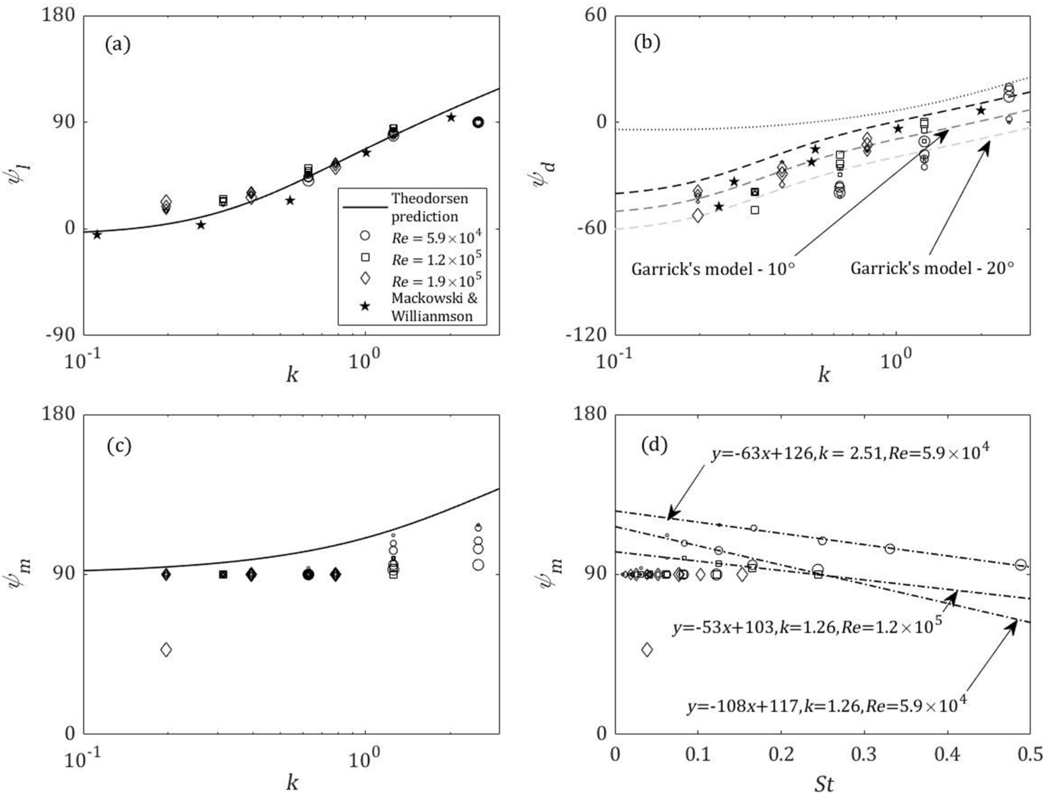

FIG. 9. Measured (a) ψ_l, (b) ψ_d, and (c) ψ_m vs k, and (d) ψ_m vs St for Re $= 5.9 \times 10^4$, 1.2×10^5, 1.9×10^5 (hollow circle, square, and diamond; size increases with α_m), compared with predictions by Theodorsen [5], Garrick [8], and Fernandez-Feria [20] (solid, dashed, and dotted lines, respectively), and with measured results by Mackowski and Williamson [35] (pentagram). Linear fitted dash-dot lines are plotted in (d).

of measured ψ_d with k is similar, but with an overall downward shift of 10°–20°. For ψ_m in Fig. 9(c), the measured values for varied α_m and Re collapse in the range of $k < 1$ and remain constant at 90° implying the independence of ψ_m from Re, k, and α_m. However, in the range of $k > 1$, the distribution with fixed k and varied α_m shows gradually increasing scatter. The plot of ψ_m versus St in Fig. 9(d) reveals a linear behavior of ψ_m with α_m at $k \geqslant 1.26$ where the RvKVS pattern dominates. The slope of the linear relation is found to increase with k and Re. In addition, a diamond symbol of $\psi_m = 48°$ at $k = 0.20$ is noted, which corresponds to the high-frequency fluctuations on the C_m' curve in the LEV case (Fig. 8, first column, bottom row) and is further discussed in Sec. III C.

C. Effect of vortex shedding regimes on the force and moment responses

In order to explore the effect of vortex shedding regimes on the force and moment responses for the purely pitching hydrofoil with the pivot located at $C/4$, i.e., the concern of question 3 raised in the introduction, this section correlates the phased-averaged vorticity fields and time series of fluctuating lift and moment coefficients over one cycle. Figures 10, 11, 12, and 13 illustrate the correlations for the three shedding regimes, LEV, UW, and RvKVS, respectively.

1. LEV regime

For the LEV regime, Fig. 10 presents the time series of the lift and moment responses (left column) and the vorticity fields at $\phi = \pi/4, \pi/2, \pi,$ and $5\pi/4$ (right column) for $k = 0.31$, $\alpha_m =$

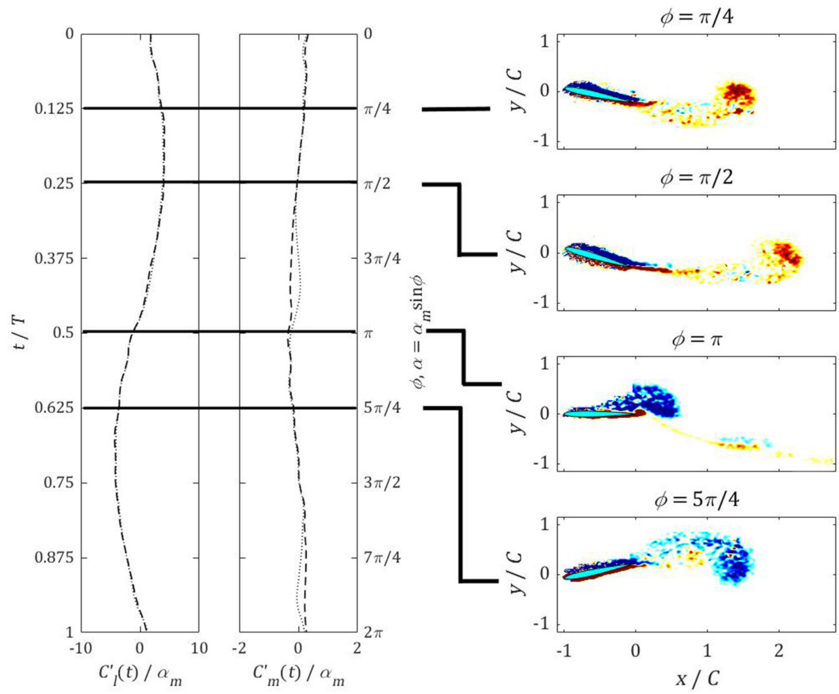

FIG. 10. Correlation of phase-averaged lift and moment responses (left, dotted lines) and vorticity fields (right, color map as in Fig. 2) for LEV pattern at $k = 0.31, \alpha_m = 24^\circ$. Lift and moment responses at $k = 0.31, \alpha_m = 16^\circ$ (left, dashed lines) are added for comparison.

24°. The lift and moment responses of $k = 0.31, \alpha_m = 16^\circ$ are added for comparison. As discussed before, superimposed high-frequency fluctuations can be identified on the C'_m curve at $k = 0.31$ and $\alpha_m = 24^\circ$. This is a dynamic stall feature, which is not observed on the C'_m curve for the UW regime at $k = 0.31$ and $\alpha_m = 16^\circ$. As the vorticity fields show, before the hydrofoil pitches from the maximum α ($\phi = \pi/2$), LEV has not formed and the moment response at $\alpha_m = 24^\circ$ collapses well with that at $\alpha_m = 16^\circ$. When the hydrofoil approaches zero α ($\phi = \pi$), the LEV is shedding off from the upper surface and convected past the trailing edge. During the period of $5\pi/8 \leqslant \phi \leqslant \pi$, the formation and convection of the LEV over the hydrofoil and the shedding of the LEV from the hydrofoil coincide with the first high-frequency fluctuation. The LEV near the hydrofoil induces a low-pressure region [42] and, thereby, the superimposed high-frequency fluctuations on the C'_m curve. With the LEV convecting further downstream in the wake, its effect on the moment response reduces.

Lift and moment responses in the case of $k = 0.16, \alpha_m = 24^\circ$ are presented in the left column of Fig. 11. On one hand, to outline the α_m effect on the LEV regime, responses in the cases of the same $k = 0.16$ and smaller $\alpha_m = 14$ and 16° are plotted for comparison. The lift responses collapse well for different α_m. However, with α_m increasing from 14° to 16°, the dynamic stall feature, i.e., high-frequency fluctuations of C'_m, begins to appear. When α_m increases up to 24°, the intensity of high-frequency C'_m fluctuations increases up to a value similar to the peak of the variation at the pitching frequency. On the other hand, the k effect on the LEV regime is derived from the comparison between Figs. 10 and 11. The intensity of high-frequency C'_m fluctuations in the case of $k = 0.16, \alpha_m = 24^\circ$ is much larger than that in the case of $k = 0.31, \alpha_m = 24^\circ$. One high-frequency C'_m fluctuation with $k = 0.31$ is observed in the phase range of $5\pi/8 \leqslant \phi \leqslant \pi$, while it is observed in a wider phase range of $\pi/2 \leqslant \phi \leqslant \pi$ with $k = 0.16$. The peak of the first fluctuation with $k = 0.31$ is located at $\phi \approx 7\pi/8$, but a phase lead of the peak is observed with $k = 0.16$. As shown in the

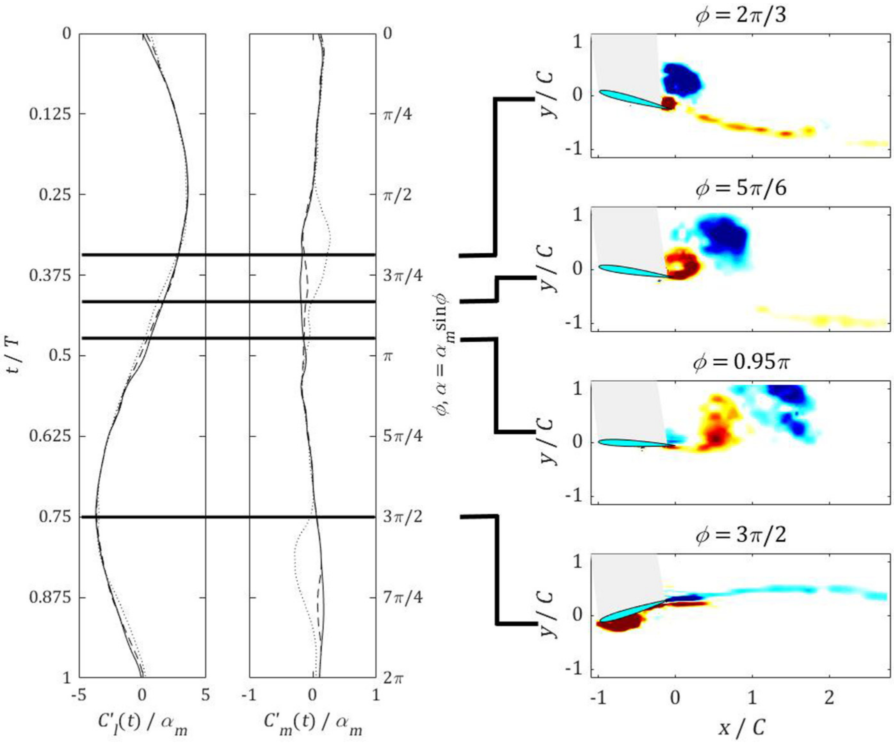

FIG. 11. Correlation of phase-averaged lift and moment responses (left, dotted lines) and vorticity fields (right, color map as in Fig. 2) for LEV pattern at $k = 0.16, \alpha_m = 24^\circ$. Lift and moment responses at $k = 0.16, \alpha_m = 14, 16^\circ$ (left, solid and dashed lines) are added for comparison. Gray regions indicate laser sheets blocked by the hydrofoil.

vorticity fields for $k = 0.16, \alpha_m = 24^\circ$ (right column of Fig. 11), the negative-vorticity LEV passes the trailing edge at $\phi = 2\pi/3$, and the first high-frequency fluctuation attains its peak value at about the same time. When a positive-vorticity trailing-edge vortex originates at $\phi = 5\pi/6$, the intensity of the high-frequency fluctuation attenuates to a weak level. Until both the negative-vorticity LEV and the positive-vorticity trailing-edge vortex are convected away from the hydrofoil at $\phi \approx \pi$, the first high-frequency fluctuation completely diminishes.

No obvious stall feature is observed on the C_l' curves of the present LEV cases with $k = 0.16, \alpha_m = 16^\circ$; $k = 0.16, \alpha_m = 24^\circ$; and $k = 0.31, \alpha_m = 24^\circ$. These LEV cases resemble a light dynamic stall in the classification of McCroskey [30]. According to the review by Corke and Thomas [3], with the flow transiting into the light dynamic stall regime, the stall feature first appears in the moment response; only when α_m increases further and the flow transits into the deep dynamic stall regime, the lift response exhibits apparent stall features. In addition, the size of the flow separation region is on the order of magnitude of the foil thickness in the light stall regime as shown in the vorticity fields at $\phi = 3\pi/2$ (Fig. 11), and increases up to the order of magnitude of the foil chord in the deep stall regime [3].

2. UW regime

For the UW pattern in Fig. 12, the time series of the lift and moment responses (left column) are correlated to the vorticity fields at $\phi = \pi/4, \pi/2, \pi,$ and $5\pi/4$ (right column) for $k = 0.63, \alpha_m = 16^\circ$. The lift and moment responses of $k = 0.63, \alpha_m = 24^\circ$ are added for comparison. At fixed $k = 0.63$, the vorticity fields of $\alpha_m = 16^\circ$ and 24° show undulating vorticity sheets with different

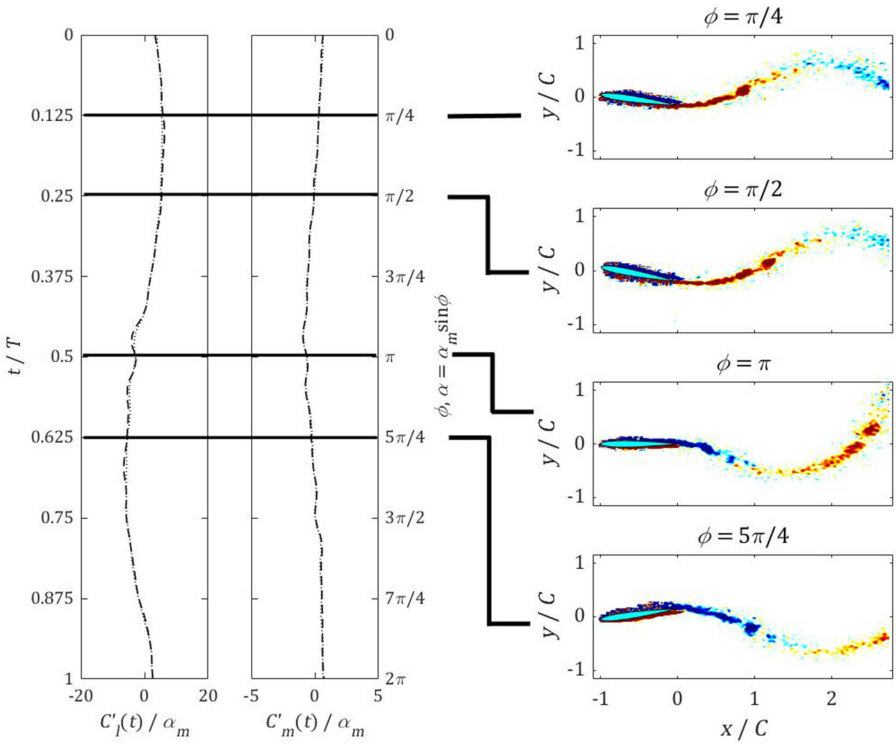

FIG. 12. Correlation of phase-averaged lift and moment responses (left, dashed lines) and vorticity fields (right, color map as in Fig. 2) for UW pattern at $k = 0.63, \alpha_m = 16^\circ$. Lift and moment responses at $k = 0.63, \alpha_m = 24^\circ$ (left, dotted lines) are added for comparison.

curvature (see the left column of Fig. 3), while the lift and moment responses collapse well. The lift and moment responses in the UW regime are locked with the foil kinematics at fixed k according to linear potential theory. In contrast, the characteristic frequency of the UW at fixed k is not fixed and decreases with increasing α_m (increasing St, see the right panel of Fig. 6). Thus, for the UW pattern the difference in the vorticity fields at different α_m does not affect the lift and moment responses significantly.

3. RvKVS regime

Figure 13 shows the correlation for the RvKVS pattern. As for the UW regime, the difference in vorticity for α_m (see the middle column of Fig. 3) only correlates with minute differences in lift and moment responses at the fixed k. The characteristic frequency of the discrete vortices in the wake of the RvKVS pattern is approximately equal to the frequency of the hydrofoil pitching for varied α_m as discussed in Sec. III A 3. In addition, the lift and moment responses are gradually decoupled from the foil kinematics, which is manifested in the increasing phase lag due to the enhanced unsteady effect with k as discussed in Sec. III B 2. It means that the vortices in the wake at fixed k and varied α_m affect little the force responses for the RvKVS pattern.

Based on the above-mentioned observations for the three regimes, the LEV effect on the force responses disappears once the LEV is shed off and convected in the wake, while the trailing-edge vortices in the wake (including the discrete vortices in the RvKVS pattern and the vorticity sheets in the UW pattern) at varied α_m and fixed k only have a minor effect on the force responses. In addition, in the trailing-edge shedding patterns, the stall feature is not observed from the force and moment responses even at $\alpha_m = 24^\circ$. This implies that dynamic stall occurs at $\alpha > 24^\circ$, considerably larger

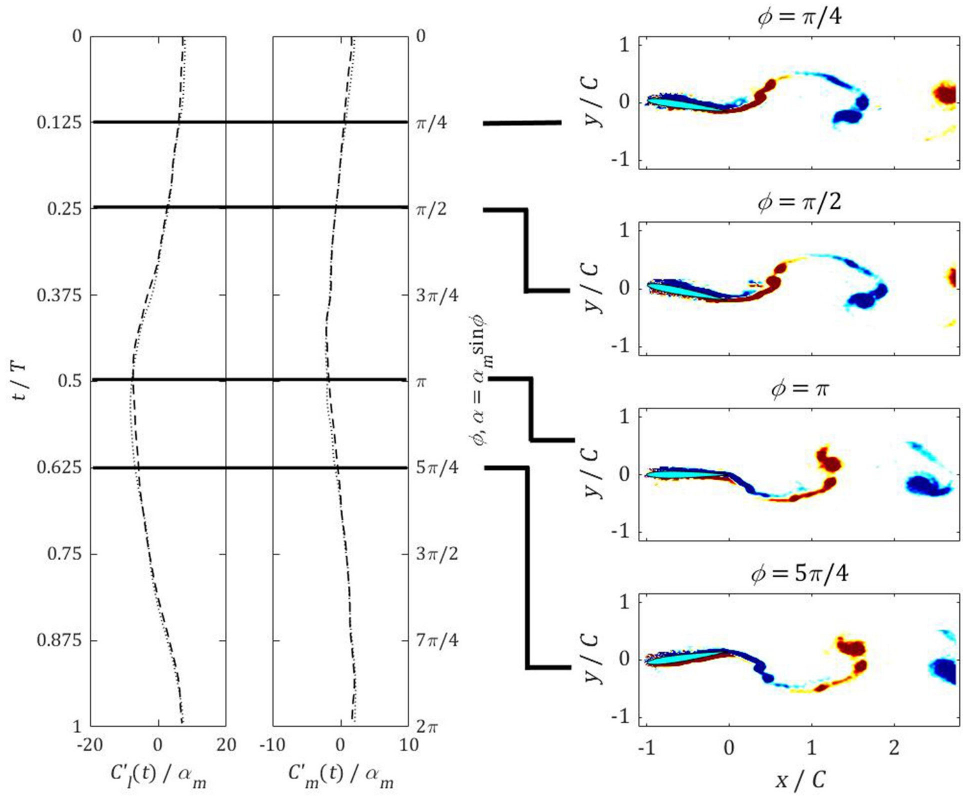

FIG. 13. Correlation of phase-averaged lift and moment responses (left, dashed lines) and vorticity fields (right, color map as in Fig. 2) for RvKVS pattern at $k = 1.26$, $\alpha_m = 16^\circ$. Lift and moment responses at $k = 1.26$, $\alpha_m = 24^\circ$ (left, dotted lines) are added for comparison.

than the static stall α of 12° for the same hydrofoil. The pitching hydrofoil thus effectively delays the stall.

IV. CONCLUSION

Targeting three questions raised in the introduction, the characteristics of vortex shedding for a sinusoidally pitching hydrofoil with the pivot location at $C/4$ were studied based on direct measurements of lift, drag, and moment, and PIV measurements of flowfields with chord Reynolds number up to 2.4×10^5 and amplitude of angle of attack up to 34°.

Three wake patterns, i.e., UW, RvKVS, and LEV, were identified from the phase-averaged vorticity fields, and were characterized for different k and α_m (see Table II). At low k and low α_m, the high Re in the present paper promotes a turbulent wake, where strongly coherent, discrete vortices are less likely to form. The result is the UW pattern instead of other complicated vortex patterns observed at low Re [34,36]. The characteristic frequency of the discrete vortex patterns (RvKVS and LEV) is approximately equal to the pitching frequency, while it differs for the UW pattern. The amplitude-based Strouhal number $\mathrm{St} = (1.5k \sin\alpha_m)/\pi$ characterizes the wake transition from UW to RvKVS pattern and the critical St is found to decrease with Re. The critical St of drag-thrust crossover is also found to decrease with Re, but remains larger than the St for wake transition to the RvKVS pattern (question 1).

Linear inviscid theory predicts $\sigma(C_l)$, $\sigma(C_m)$, $\overline{C_d}$, and $\sigma(C_d)$ well up to $\alpha_m \leqslant 12^\circ$, but the discrepancy due to the nonlinear effect gradually increases with increasing α_m. With the flow attached, the viscous effect leads to a larger variability of the measured values for low k. With increasing Re, the measured values gradually approach the theoretical prediction. More accurate prediction of the time-dependent response than that by linear inviscid theory requires a deep understanding of the phase lag between the dynamic force and the hydrofoil kinematics. The phase lags serve as an indicator of the decoupling between force response and hydrofoil kinematics due to the inertial effect in the increasingly unsteady flow with k. Linear inviscid theory only provides a good prediction of ψ_l for $k \leqslant 2$. For ψ_d and ψ_m, linear inviscid theory cannot capture the α_m-dependent behavior and deviates comparatively far from the measured values. A linear relation of ψ_m versus α_m (i.e., ψ_m versus St at fixed $k \geqslant 1.26$) is found for varied k and Re (question 2).

For the LEV regime at low k and high α_m, the signature of LEV over the hydrofoil is clearly identified from the unsteady pitching moment (not lift or drag) as a light stall. However, this is not the case for the UW and RvKVS regimes, where the force and moment responses are largely insensitive to vorticity sheets of the UW pattern and discrete vortices of the RvKVS pattern at varied α_m. Within the trailing-edge shedding regimes, the flow remains attached on the hydrofoil up to $\alpha_m = 24^\circ$ and the pitching motion effectively delays the stall (question 3).

Finally, one limitation to the present paper should be noted. The vortex shedding discussed here pertains to a pivot location at $C/4$. The effect of pivot location on the wake patterns may warrant further study.

ACKNOWLEDGMENTS

This work was supported by the National Key Research and Development Plan of China (Grants No. 2017YFE0132000 and No. 2018YFB1501202), the National Natural Science Foundation of China (Grant No. 11872248), and the Self-directed Research Subject of the State Key Laboratory of Marine Engineering in Shanghai Jiao Tong University (Grant No. GKZD010075). The authors would like to thank the engineers J. Gong, F. Wei, Y. Dai, and F. Wang, and the postgraduates C. Tu and W. Xu, for their assistance and support throughout the course of experiments.

APPENDIX A: EXPERIMENTAL PARAMETER TABLE FOR THE PITCHING HYDROFOIL

In the present experiment, the unsteady hydrodynamics of the sinusoidally pitching NACA 0012 hydrofoil is studied by the force measurement and the PIV measurement, with different freestream velocity U, hydrofoil pitching frequency f, and amplitude α_m. These physical parameters and the resulting dimensionless parameters of the chord Reynolds number Re, the reduced frequency k, and the amplitude-based Strouhal number St are summarized in Table III.

APPENDIX B: PREDICTION BY LINEAR POTENTIAL THEORY

Theodorsen [5] modeled the unsteady lift and moment of a thin flat plate and a flat vortical wake in incompressible flow with the argument of reduced frequency k. For the symmetric hydrofoil pitching with zero mean α and about $C/4$ pivot point location, Theodorsen theory gives the dynamic lift coefficient in complex form:

$$2\pi\left(\alpha + \frac{C\dot{\alpha}}{2U}\right)\mathrm{TF}(k) + \frac{\pi}{2}\left(\frac{C\dot{\alpha}}{U} + \frac{C^2\ddot{\alpha}}{4U^2}\right), \tag{B1}$$

where the first term models the circulatory effects and the second term is the apparent mass term or noncirculatory lift due to acceleration effect. In the circulatory term, TF(k) is the complex-valued Theodorsen function. The noncirculatory term follows instantaneously the kinematics of motion and is progressively larger for larger k. The dynamic moment coefficient about the $C/4$ pivot point is predicted by Theodorsen theory as the complex form of

$$-\frac{\pi}{4}\left(\frac{C\dot{\alpha}}{U} + \frac{3C^2\ddot{\alpha}}{16U^2}\right). \tag{B2}$$

TABLE III. Experimental parameter settings for the sinusoidally pitching hydrofoil.

U (m/s)	f (Hz)	α_m (deg)	Re	k	St	Force measurement	PIV measurement
0.25	0.25	6	5.9×10^4	0.63	0.031	✓	
0.25	0.25	8	5.9×10^4	0.63	0.042	✓	✓
0.25	0.25	12	5.9×10^4	0.63	0.062	✓	
0.25	0.25	16	5.9×10^4	0.63	0.083	✓	✓
0.25	0.25	24	5.9×10^4	0.63	0.122	✓	✓
0.25	0.5	6	5.9×10^4	1.26	0.063	✓	
0.25	0.5	8	5.9×10^4	1.26	0.084	✓	
0.25	0.5	12	5.9×10^4	1.26	0.125	✓	
0.25	0.5	16	5.9×10^4	1.26	0.165	✓	
0.25	0.5	24	5.9×10^4	1.26	0.244	✓	
0.25	1.0	6	5.9×10^4	2.51	0.125	✓	
0.25	1.0	8	5.9×10^4	2.51	0.167	✓	✓
0.25	1.0	12	5.9×10^4	2.51	0.250	✓	
0.25	1.0	16	5.9×10^4	2.51	0.331	✓	✓
0.25	1.0	24	5.9×10^4	2.51	0.488	✓	✓
0.5	0.25	6	1.2×10^5	0.31	0.016	✓	
0.5	0.25	8	1.2×10^5	0.31	0.021	✓	✓
0.5	0.25	12	1.2×10^5	0.31	0.031	✓	
0.5	0.25	16	1.2×10^5	0.31	0.041	✓	✓
0.5	0.25	24	1.2×10^5	0.31	0.061	✓	✓
0.5	0.25	34	1.2×10^5	0.31	0.084	✓	✓
0.5	0.5	6	1.2×10^5	0.63	0.031	✓	
0.5	0.5	8	1.2×10^5	0.63	0.042	✓	
0.5	0.5	12	1.2×10^5	0.63	0.062	✓	
0.5	0.5	16	1.2×10^5	0.63	0.083	✓	
0.5	0.5	24	1.2×10^5	0.63	0.122	✓	
0.5	1.0	6	1.2×10^5	1.26	0.063	✓	
0.5	1.0	8	1.2×10^5	1.26	0.084	✓	✓
0.5	1.0	12	1.2×10^5	1.26	0.125	✓	
0.5	1.0	16	1.2×10^5	1.26	0.165	✓	✓
0.5	1.0	24	1.2×10^5	1.26	0.244	✓	✓
0.8	0.25	6	1.9×10^5	0.20	0.010	✓	
0.8	0.25	8	1.9×10^5	0.20	0.013	✓	
0.8	0.25	12	1.9×10^5	0.20	0.020	✓	
0.8	0.25	16	1.9×10^5	0.20	0.026	✓	
0.8	0.25	24	1.9×10^5	0.20	0.038	✓	
0.8	0.5	6	1.9×10^5	0.39	0.020	✓	
0.8	0.5	8	1.9×10^5	0.39	0.026	✓	
0.8	0.5	12	1.9×10^5	0.39	0.039	✓	
0.8	0.5	16	1.9×10^5	0.39	0.052	✓	
0.8	0.5	24	1.9×10^5	0.39	0.076	✓	
0.8	1.0	6	1.9×10^5	0.79	0.039	✓	
0.8	1.0	8	1.9×10^5	0.79	0.052	✓	
0.8	1.0	12	1.9×10^5	0.79	0.078	✓	
0.8	1.0	16	1.9×10^5	0.79	0.103	✓	
0.8	1.0	24	1.9×10^5	0.79	0.153	✓	
1.0	0.25	14	2.4×10^5	0.16	0.018	✓	
1.0	0.25	16	2.4×10^5	0.16	0.021	✓	
1.0	0.25	24	2.4×10^5	0.16	0.031	✓	✓

It is worth noting that both the circulatory and noncirculatory parts contribute to the lift response, but only the noncirculatory part contributes to the moment response.

In the implementation of prediction by Theodorsen theory, the sinusoidal pitch input is in the complex form of $\alpha_m e^{i\omega t}$. Then, the dynamic lift and moment coefficients, respectively, simplify to

$$[2\pi\alpha_m \mathrm{TF}(k)(1+ik) + \pi\alpha_m(ik - k^2/2)]e^{i\omega t}, \tag{B3}$$

and

$$2\pi\alpha_m(-ik/4 + 3k^2/32)e^{i\omega t}. \tag{B4}$$

The exact expression of $\mathrm{TF}(k)$ is given in terms of the Bessel functions of the third kind, i.e., Hankel function, of orders zero and one, $H_0(k)$ and $H_1(k)$:

$$\mathrm{TF}(k) = \frac{H_1(k)}{H_1(k) + iH_0(k)} = F(k) + iG(k). \tag{B5}$$

Because the hydrofoil motion $\alpha(t) = \alpha_m \sin(\omega t)$ is the imaginary part of $\alpha_m e^{i\omega t}$, the dynamic lift and moment coefficients should be the corresponding imaginary part:

$$C_l(t) = 2\pi\alpha_m M_l \sin(\omega t + \psi_l), \tag{B6}$$

$$C_m(t) = 2\pi\alpha_m M_m \sin(\omega t + \psi_m), \tag{B7}$$

where

$$M_l(k) = \sqrt{(-k^2/4 + F - kG)^2 + (k/2 + kF + G)^2},$$

$$\psi_l(k) = \arctan\left(\frac{k/2 + kF + G}{-k^2/4 + F - kG}\right),$$

$$M_m(k) = \frac{k}{4}\sqrt{1 + \frac{9k^2}{64}},$$

$$\psi_m(k) = -\arctan\left(\frac{8}{3k}\right).$$

Here, the explicit relation of the lift and moment response to sinusoidal α variation is constructed as a function of α_m and k. It is noted that the mean values of the dynamic lift and moment coefficients $\overline{C_l}$ and $\overline{C_m}$ vanish to zero.

Based on the analyses by Theodorsen [5] for unsteady lift and by von Kármán and Burgers [9] for streamwise force, Garrick [8] proposed the model of drag response to sinusoidal oscillation:

$$C_d(t) = C_d^l + C_d^v. \tag{B8}$$

The first term C_d^l is the streamwise projection of the lift force normal to the foil:

$$C_d^l = \alpha(t) \times C_l(t) = \pi\alpha_m^2 M_l[\cos(\psi_l) - \cos(2\omega t + \psi_l)]. \tag{B9}$$

The second term C_d^v is the leading-edge suction force which is produced by the vorticity distribution. The leading-edge suction term simplifies to

$$C_d^v = -\pi\alpha_m^2 M_d^{v2}\big[1 - \cos 2\big(\omega t + \psi_d^v\big)\big]/2, \tag{B10}$$

where

$$M_d^{v2} = [(2F - 2kG)^2 + (2kF + 2G - k)^2]/2,$$

$$\psi_d^v = \arctan\left(\frac{2kF + 2G - k}{2F - 2kG}\right).$$

Accordingly, the dynamic drag coefficient can be decomposed into two parts: the mean component

$$\overline{C_d} = \pi\alpha_m^2[(1 + k^2)[F - (F^2 + G^2)] - k^2/2], \tag{B11}$$

and the fluctuating component

$$C_d' = \pi\alpha_m^2 M_d \sin 2(\omega t + \psi_d), \tag{B12}$$

where

$$M_d^2 = M_l^2 + M_d^{v4}/4 - M_l M_d^{v2}\cos\left(2\psi_d^v - \psi_l\right),$$

$$2\psi_d = \arctan\left[\frac{2M_l - M_d^{v2}\cos\left(2\psi_d^v - \psi_l\right)}{M_d^{v2}\sin\left(2\psi_d^v - \psi_l\right)}\right] + \psi_l.$$

Garrick [8] considered only the leading-edge suction, in addition to the pressure force projection along the streamwise direction. In order to get an improved model, Fernandez-Feria [20] used the vortical impulse theory to consider the effect of wake vorticity all over the foil and not only at the leading edge. In Fernandez-Feria's model, the drag coefficient was written as

$$C_d(t) = C_d^l + C_{d2} + C_{d3}. \tag{B13}$$

The first term related to the streamwise projection of pressure force is identical to that in Garrick's model. The two latter terms are, respectively, the apparent mass term C_{d2} and the wake-related term C_{d3}. For the hydrofoil motion $\alpha(t) = \alpha_m \sin(\omega t)$ about the $C/4$ pivot point, the apparent mass term simplifies to

$$C_{d2} = \overline{C_{d2}} + \pi\alpha_m^2 M_{d2}\sin(2\omega t + \psi_{d2}), \tag{B14}$$

where

$$\overline{C_{d2}} = \pi\alpha_m^2 k^2/4,$$

$$M_{d2}(k) = \frac{k}{2}\sqrt{1 + \frac{k^2}{4}},$$

$$\psi_{d2}(k) = \arctan\left(\frac{k}{2}\right).$$

The wake-effect-related term is

$$C_{d3} = -4\mathrm{Im}\{(1 + ik)\alpha_m e^{i\omega t}\} \times \mathrm{Im}\{[(-3k/2 + 2i)\mathrm{FF}(k) - \pi\mathrm{TF}(k)/2]\alpha_m e^{i\omega t}\}, \tag{B15}$$

where Im{} is the imaginary part of a complex and FF(k) is another complex-value function:

$$\mathrm{FF}(k) = \frac{e^{-ik}/k}{H_1(k) + iH_0(k)} = F_1(k) + iG_1(k). \tag{B16}$$

The expression of the wake-related term in real form simplifies to

$$C_{d3} = \overline{C_{d3}} + \alpha_m^2 M_{d3}\sin(2\omega t + \psi_{d3}), \tag{B17}$$

where

$$\overline{C_{d3}} = \alpha_m^2[-kF_1 + (3k^2+4)G_1 + \pi(F+kG)],$$

$$M_{d3}(k) = \mathrm{sqrt}\{[(3k^2-4)F_1 + 7kG_1 + \pi(kF+G)]^2 + [-7kF_1 + (3k^2-4)G_1 - \pi(F-kG)]^2\},$$

$$\psi_{d3}(k) = \arctan\left[\frac{-7kF_1 + (3k^2-4)G_1 - \pi(F-kG)}{(3k^2-4)F_1 + 7kG_1 + \pi(kF+G)}\right].$$

Then, the mean value of the drag coefficient in Fernandez-Feria's model is the sum of mean values of C_d^l, C_{d2}, and C_{d3}:

$$\overline{C_d} = \alpha_m^2[2\pi F - kF_1 + (3k^2+4)G_1]. \tag{B18}$$

Similarly, the fluctuating component of the drag coefficient is

$$C_d' = \pi\alpha_m^2 M_d \sin 2(\omega t + \psi_d), \tag{B19}$$

where

$$M_d = \mathrm{sqrt}\left\{\left[\frac{(3k^2-4)F_1 + 7kG_1}{\pi} + 2(kF+G) + k\right]^2 + \left[\frac{-7kF_1 + (3k^2-4)G_1}{\pi} - 2(F-kG) + k^2/2\right]^2\right\},$$

$$2\psi_d = \arctan\left[\frac{-7kF_1 + (3k^2-4)G_1 - 2\pi(F-kG) + \pi k^2/2}{(3k^2-4)F_1 + 7kG_1 + 2\pi(kF+G) + \pi k}\right].$$

[1] W. R. Hawthorne and R. A. Novak, The aerodynamics of turbo-machinery, Annu. Rev. Fluid Mech. **1**, 341 (1969).

[2] Y. Li, J. Yi, H. Song, Q. Wang, Z. Yang, N. D. Kelley, and K.-S. Lee, On the natural frequency of tidal current power systems - A discussion of sea testing, Appl. Phys. Lett. **105**, 023902 (2014).

[3] T. C. Corke and F. O. Thomas, Dynamic stall in pitching airfoils: Aerodynamic damping and compressibility effects, Annu. Rev. Fluid Mech. **47**, 479 (2015).

[4] S. Li, Y. Li, C. Yang, Q. Wang, B. Zhao, D. Li, R. Zhao, T. Ren, X. Zheng, Z. Gao, and W. Xu, Experimental investigation of solidity and other characteristics on dual vertical axis wind turbines in an urban environment, Energ. Convers. Manage. **229**, 113689 (2021).

[5] T. Theodorsen, General theory of aerodynamic instability and the mechanism of flutter, NACA Technical Report No. 496, 1979.

[6] W. R. Sears, A systematic presentation of the theory of thin airfoils in non-uniform motion, Ph.D. thesis, California Institute of Technology, 1938.

[7] T. H. von Kármán and W. R. Sears, Airfoil theory for non-uniform motion, J. Aeronaut. Sci. **5**, 379 (1938).

[8] I. E. Garrick, Propulsion of a flapping and oscillating airfoil, NACA Technical Report No. 567, 1936.

[9] T. H. von Kármán and J. M. Burgers, *General Aerodynamic Theory: Perfect Fluids* (Springer, New York, 1935).

[10] M. D. van Dyke, Supersonic flow past oscillating airfoils including nonlinear thickness effects, NACA Technical Report No. 2982, 1953.

[11] W. J. McCroskey and J. J. Philippe, Unsteady viscous flow on oscillating airfoils, AIAA J. **13**, 71 (1975).

[12] W. J. McCroskey and S. L. Pucci, Viscous-inviscid interaction on oscillating airfoils in subsonic flow, AIAA J. **20**, 167 (1982).
[13] J. M. Anderson, K. Streitlien, D. S. Barrett, and M. S. Triantafyllou, Oscillating foils of high propulsive efficiency, J. Fluid Mech. **360**, 41 (1998).
[14] K. Ramesh, A. Gopalarathnam, K. Granlund, M. V. Ol, and J. R. Edwards, Discrete-vortex method with novel shedding criterion for unsteady aerofoil flows with intermittent leading-edge vortex shedding, J. Fluid Mech. **751**, 500 (2014).
[15] J. Li and Z. N. Wu, Vortex force map method for viscous flows of general airfoils, J. Fluid Mech. **836**, 145 (2018).
[16] R. Fernandez-Feria and J. Alaminos-Quesada, Unsteady thrust, lift and moment of a two-dimensional flapping thin airfoil in the presence of leading-edge vortices: A first approximation from linear potential theory, J. Fluid Mech. **851**, 344 (2018).
[17] A. Martín-Alcántara and R. Fernandez-Feria, Assessment of two vortex formulations for computing forces of a flapping foil at high Reynolds numbers, Phys. Rev. Fluids **4**, 024702 (2019).
[18] X. Xia and K. Mohseni, Unsteady aerodynamics and vortex-sheet formation of a two-dimensional airfoil, J. Fluid Mech. **830**, 439 (2017).
[19] J. Li, Y. Wang, M. Graham, and X. Zhao, Vortex moment map for unsteady incompressible viscous flows, J. Fluid Mech. **891**, A13 (2020).
[20] R. Fernandez-Feria, Linearized propulsion theory of flapping airfoils revisited, Phys. Rev. Fluids **1**, 084502 (2016).
[21] W. R. Graham, C. P. Ford, and H. Babinsky, An impulse-based approach to estimating forces in unsteady flow, J. Fluid Mech. **815**, 60 (2017).
[22] L. Kang, L. Liu, W. Su, and J. Wu, A minimum-domain impulse theory for unsteady aerodynamic force with discrete wake, Theor. Appl. Mech. Lett. **7**, 306 (2017).
[23] M. S. Triantafyllou, A. H. Techet, and F. S. Hover, Review of experimental work in biomimetic foils, IEEE J. Oceanic Eng. **29**, 585 (2004).
[24] Q. Zhu and K. Shoele, Propulsion performance of a skeleton-strengthened fin, J. Exp. Biol. **211**, 2087 (2008).
[25] Q. Zhu, Y. Liu, and D. K. P. Yue, Dynamics of a three-dimensional oscillating foil near the free surface, AIAA J. **44**, 2997 (2006).
[26] J. T. King, R. Kumar, and M. A. Green, Experimental observations of the three-dimensional wake structures and dynamics generated by a rigid, bioinspired pitching panel, Phys. Rev. Fluids **3**, 034701 (2018).
[27] M. V. Ol, High-frequency, high-amplitude pitch problem: Airfoils, plates, and wings, in *Proceedings of the 39th AIAA Fluid Dynamics Conference* (AIAA, Reston, VA, 2009), paper no. AIAA 2009-3686.
[28] Y. Yu, X. Amandolese, C. Fan, and Y. Liu, Experimental study and modelling of unsteady aerodynamic forces and moment on flat plate in high amplitude pitch ramp motion, J. Fluid Mech. **846**, 82 (2018).
[29] U. Cordes, G. Kampers, T. Meißner, C. Tropea, J. Peinke, and M. Hölling, Note on the limitations of the Theodorsen and Sears functions, J. Fluid Mech. **811**, R1 (2017).
[30] W. J. McCroskey, Unsteady airfoils, Annu. Rev. Fluid Mech. **14**, 285 (1982).
[31] M. M. Koochesfahani, Vortical patterns in the wake of an oscillating airfoil, AIAA J. **27**, 1200 (1989).
[32] M. L. Rueger and G. M. Gregorek, An experimental investigation of the effect of vortex generators on the aerodynamic characteristics of a NACA0021 airfoil undergoing large amplitude pitch oscillations, Sandia National Laboratories, Technical Report No. SAND-90-7111 ON: DE91012102, 1991.
[33] D. G. Bohl and M. M. Koochesfahani, MTV measurements of the vortical field in the wake of an airfoil oscillating at high reduced frequency, J. Fluid Mech. **620**, 63 (2009).
[34] T. Schnipper, A. Andersen, and T. Bohr, Vortex wakes of a flapping foil, J. Fluid Mech. **633**, 411 (2009).
[35] A. W. Mackowski and C. H. K. Williamson, Direct measurement of thrust and efficiency of an airfoil undergoing pure pitching, J. Fluid Mech. **765**, 524 (2015).
[36] A. Andersen, T. Bohr, T. Schnipper, and J. H. Walther, Wake structure and thrust generation of a flapping foil in two-dimensional flow, J. Fluid Mech. **812**, R4 (2017).

[37] S. Yamada, T. Tamura, and S. Mochizuki, Effects of end plates on performance of a small straight-bladed vertical axis wind turbine, J. Fluid Sci. Tech. **12**, JFST0019 (2017).

[38] Y. Li and S. M. Calisal, Three-dimensional effects and arm effects on modeling a vertical axis tidal current turbine, Renewable Energy **35**, 2325 (2010).

[39] M. Raffel, C. E. Willert, F. Scarano, C. J. Kähler, S. T. Wereley, and J. Kompenhans, Image evaluation methods for PIV, in *Particle Image Velocimetry: A Practical Guide* (Springer, New York, 2018).

[40] J. S. Bendat and A. G. Piersol, Statistical principles, in *Random Data: Analysis and Measurement Procedures*, 4th ed. (Wiley, New York, 2010).

[41] J. C. Hunt, A. A. Wray, and P. Moin, Eddies, streams, and convergence zones in turbulent flows, in *Proceedings of the 1988 Summer Program Studying Turbulence Using Numerical Simulation Databases* (Center for Turbulence Research, Stanford University, 1988), pp. 193–209.

[42] J. Jeong and F. Hussain, On the identification of a vortex, J. Fluid Mech. **285**, 69 (1995).

[43] P. Chakraborty, S. Balachandar, and R. J. Adrian, On the relationships between local vortex identification schemes, J. Fluid Mech. **535**, 189 (2005).

[44] S. Tian, Y. Gao, X. Dong, and C. Liu, Definitions of vortex vector and vortex, J. Fluid Mech. **849**, 312 (2018).